2018-01-01

Development Of A Desktop Material Extrusion 3d Printer With Wire Embedding Capabilities

Jose Francisco Motta
University of Texas at El Paso, pacomotta32@gmail.com

DEVELOPMENT OF A DESKTOP MATERIAL EXTRUSION 3D PRINTER WITH WIRE EMBEDDING CAPABILITIES

JOSE FRANCISCO MOTTA

Master's Program in Mechanical Engineering

APPROVED:

David Espalin, Ph.D.

Ryan Wicker, Ph.D.

Amit J. Lopes, Ph.D.

Charles Ambler, Ph.D.
Dean of the Graduate School

Dedication

This thesis is dedicated to my mother, brother, family and friends for their immense motivation and support throughout my academic studies.

DEVELOPMENT OF A MATERIAL EXTRUSION DESKTOP 3D PRINTER WITH WIRE EMBEDDING CAPABILITIES

by

JOSE FRANCISCO MOTTA, B.Sc

THESIS

Presented to the Faculty of the Graduate School of

The University of Texas at El Paso

in Partial Fulfillment

of the Requirements

for the Degree of

MASTER OF SCIENCE

Department of Mechanical Engineering

THE UNIVERSITY OF TEXAS AT EL PASO

December 2018

ACKNOWLEDGEMENTS

I would like to thank Dr. Ryan Wicker, director of the W.M. Keck Center for 3D innovation, for allowing me to fully immerse myself in additive manufacturing by utilizing the high-end research equipment that the Keck Center has to offer. I would also like to express my greatest gratitude to my mentor, Dr. David Espalin, for the massive support throughout my undergraduate and graduate studies. Dr. Espalin helped me grow both academically and professionally by challenging me to think outside the box when solving a difficult problem. Also, I wish to recognize Jose Coronel for all his input on the development of the modular desktop 3D printer. Additionally, I would like to thank all the faculty and staff that contributed on this project.

Special thanks to Mr. Christopher Minjares for his enormous time commitment during machining most of the components used to assemble the system. I would also like to thank Dr. Chiyen Kim and Mr. Xavier Jimenez for their contribution and support on the development of the controls of the system. I would also like to thank the following graduate and undergraduate students of the Keck Center, Mr. Jorge Ramirez, Mr. Alfonso Fernandez, Mr. Kazi Md Masum Billah, Mr. Adrian Belmontes, Mr. Angel Vega, Ms. Sol Barraza, Mr. Judah Lesser, and Mr. Brandon Fischer for their contribution on this project.

I wish to thank my girlfriend, Ana, for her understanding, love, and support throughout my graduate studies. Finally, I am thankful for my wonderful mother, brother, and family that inspired me to grow and challenge myself to always achieve my goals.

ABSTRACT

Printed circuit boards (PCB) have been widely used as a permanent solution for generating complex circuitries to power electronic devices. Over the years, PCB boards have proved to be reliable when powering electronic devices. However, when fabricating a printed circuit board, one must outsource to fabricate the boards when in prototype phase. Therefore, the risk of intellectual property theft and long lead time is an issue. The objective of this thesis is to develop a hybrid multi-tool desktop material extrusion 3D printer that allows for easy integration (modularity) of tools to generate multi-functional 3D printed components.

The addition of an ultrasonic wire embedding tool allowed for embedding of conductive wires (traces) intended for interconnection between electronic components on 3D printed parts. Additionally, the implementation of tools, such as machining, has the potential to enhance extra feature resolution that is not achievable by material extrusion itself. Experiments were performed to understand the limitations of the modular desktop 3D printer and inform the user of design parameters and constraints for material extrusion and wire embedding. Repeatability tests of the XYZ axes were performed to understand the resolution of the modular desktop 3D printer. As a result, the deviation of the Y-axis was ±0.5μm with an average error of 0.11% for a 5mm travel displacement based on 10 measurements. Similarly, the X- and Z-axis showed a deviation for both a 2mm and a 5mm travel displacements of ±1.63 μm and ±0.78 μm with a percent error of 0.18% and 0.16%, respectively.

A computational steady state heat transfer analysis, validated by an experimental setup, was developed to understand the temperature distribution of the build platform. The computational analysis showed a maximum temperature of ~84ºC using a power input of 200W. To validate the computational analysis, an IR camera and a thermocouple data acquisition system measured the temperature of the build platform. The IR and thermocouple near the heat source reached 120ºC (set temperature) in approximately 8 minutes. The sensor located on the surface of the build

platform 15.24cm (6in) away from the heat source reached a steady temperature of 101ºC in 14 minutes when the built platform was set to 120ºC.

To characterize the material extrusion of the modular desktop 3D printer, an extruder gear ratio of 1:30 was determined by trial error. Different line sizes were printed and measured ten times with a digital caliper to compare the set lengths with the actual extruded lengths. The extruded lines set to 10mm and 150mm measured 10.34±0.64mm and 151.93±0.58mm, respectively. After obtaining the extruder gear ratio, a ranking model inspired by Moylan *et al.* (2012) was used to compare the part dimensional accuracy of the modular desktop 3D printer with an industry grade Fortus 400mc (Stratasys, Eden Prairie, MN) FDM printer. With the help of an optical measuring tool, 25 features were measured for a PLA ranking model produced by the modular desktop 3D printer and a PC ranking model produced by the FDM 3D printer. Both parts showed undersized and oversized features at different locations. However, the largest oversized feature was produced by the modular desktop 3D printer having a percent error of 1.46% compared to the 0.02% error produced by the FDM for the same feature. That is, the difference from the feature size of the CAD model to actual printed feature was 1.12mm.

Parameters for wire embedding were developed using trial and error by varying the amplitude and traversing speed of the wire embedding tool. Embedding 26AWG solid copper wire onto an ABS plastic substrate required an amplitude of 60% at an embedding speed of 8mm/s. To characterize the wire embedding, three linear pairs of parallel traces were embedded with a center-to-center distance of 10mm, 1mm, and 0.5mm. Using an optical measuring tool, the center-to-center distances for the linear pairs were 10.31mm, 1.16mm, and 0.70mm. Finally, to understand the variance of the center-to-center distance between two parallel wires with angles, four fully dense ABS plastic substrates were printed and three different trace pairs varying in width with a sharp turn of 135º, 90º, 60º, 35º were fabricated. Complete failure of embedding the 35º turn was seen due to excessive amount of accumulated energy input in the same area as the wire was not retained by the polymer due the polymer flow when excessive energy was accumulated. This allowed for the development of design constraints, for example, a spacing of approximately 6mm

was experimentally calculated to avoid interference with the component/feature when placed close to a wire trace with a sharp turn.

Machining capabilities were easily integrated to the modular desktop 3D printer. A rectangular ABS coupon was faced using a 1/8 end mill at a federate of 8mm/s to prove for easy integration of other tools. The system allowed a maximum payload of 86 kg (190lbs) when the load was at the center of the Z stage.

TABLE OF CONTENTS

LIST OF TABLES

LIST OF FIGURES

CHAPTER 1

INTRODUCTION

Additive manufacturing (AM) has been recognized for its ability to generate complex parts with the help of a layer-by-layer process directly from a 3D computer-aided design (CAD) model. This novel technology has been integrated in the industry to generate prototypes faster when compared to traditional manufacturing methods such as plastic injection or machining. Other industries have adapted AM to directly and indirectly produce massive quantities of personalized parts such as custom hearing aids, dental aligners, and molds to replicate a part many times. However, a technology gap is greatly noticeable when 3D printed parts require additional functionalities other than simply structural and aesthetics.

1.1. MOTIVATION

To enable the integration of multiple tools with the material extrusion AM process, a method for embedding wire onto material extrusion-printed parts was investigated and implemented on a novel easy-to-transport 3D printer. The printer was developed and constructed with the aim of having complete modularity for multiple tool integration. Access to multiple tools is viewed as a benefit because the strengths of each tool can be leveraged to generate improved parts. As an example, material extrusion AM can produce complex parts relatively quickly, but with limited feature resolution. The integration of machining capabilities can therefore realize feature resolution or surface roughness to meet final application requirements. In response to this motivation, the following objectives were identified.

1.2. THESIS OBJECTIVES

- Develop a modular desktop 3D printer with multiple tool integration capabilities to generate multi-functional printed components
- Test and characterize the system to understand its capabilities when compared to industry standard 3D printers

- Obtain parameters for material extrusion and characterize the 3D printed part
- Obtain parameters for wire embedding and characterize the wire embedding on a 3D printed part

CHAPTER 2

LITERATURE REVIEW

2. SEVEN PROCESSES OF ADDITIVE MANUFACTURING

Additive manufacturing, also known as 3D printing, is a process in which a virtual 3D model is sliced into 2D cross-sections and converted to machine language to fabricate a part. The AM machine merges the 2D cross-sections and builds in a layer-by-layer sequence to completely fabricate a 3D physical part (Gibson *et al.*, 2015). There are seven processes that use the layer-by-layer approach to produce geometries of high complexity, allow for greater material efficiency, and provide the ability to combine materials that would be impossible to combine with traditional manufacturing methods, such as subtractive manufacturing. The currently available AM processes are material extrusion, vat-photopolymerization, sheet lamination, binder jetting, powder bed fusion, material jetting, and direct energy deposition.

Gibson *et al* described the seven printing processes as follows:

1. vat-photopolymerization process consists of a moving platform that is submerged into a vat of liquid photopolymer. UV light is used to cure different sections to form the 2D plane. The moving platform shifts upward at the completion of each layer, and the process is repeated to form a 3D part.
2. powder bed fusion process uses a container filled with powder and with the help of an energy source, a scanning laser or electron beam, selectively melts the powder to form a layer. The powder container is lowered, and with the help of a rake or roller, material powder is distributed along the surface and the process is repeated.
3. material extrusion is the process in which material is extruded through a nozzle in a scanning pattern to procedure a cross-section of the 3D printed part.
4. material jetting uses conventional paper ink-jet printing followed by UV light to cure the jetted material to provide 2D cross-sections.

5. binder jetting is the process in which a binder agent is deposited onto a powder bed to form the 2D cross-sections of the 3D part.
6. sheet lamination is the process in which a sheet is sectioned with a form-then-cut or a cut-then-form process to shape the 3D part.
7. directed energy deposition is the process in which material in the form of powder or wire is fed to an energy source to create the 2D cross-sections of the 3D part.

Table 1 Typical materials in AM processes

AM Process	Typical material class
Vat-photopolymerization	UV curable resin, acrylic plastic
Powder bed fusion	Metals, thermoplastics
Material Extrusion	Thermoplastics
Material jetting	Polymers
Binder jetting	Metals, ceramics, polymers
Sheet lamination	Polymer, metals, wood, glass
Directed energy deposition	Metals

Table 1 shows a summary of materials that may be used for each of the seven AM processes. Some uses for the seven processes of AM are in medicine such as hip implants made by electron beam melting (EBM) or using stereolithography (SL) to produce individual aligners from a scan of a patient to align their teeth (Quinlan, 2017). AM can reduce production cost of a component at its prototype phase and in most cases, reduce lead time. Quinlan *et al.* compared powder bed laser melting (LM) process to traditional manufacturing CNC and discovered a trend

that he states as “complexity for the same cost as simplicity”. This implies that as the geometry complexity of the stainless-steel part increased, the cost of the LM-produced part did not, instead, the cost per part decreased when complexity was added. In contrast, the CNC-produced cost per part increased as the complexity level increased. Quinlan *et al.* also investigated the applications of how companies like PepsiCo are implementing 3D printing to test, for example, printed prototypes of potato chips to judge the tactical feel, quality, and aesthetics. GE and Siemens have been using LM and EBM to develop jet engine components and increase efficiency of gas burners (Quinlan, 2017). Similarly, ORNL is using binder jetting to produce high-performance rare-earth magnets (Quinlan, 2017).

2.1. Material Extrusion

Material Extrusion is one of the most popular processes of the existing seven AM processes for prototyping due to its fast machine setup when compared to the other processes. A polymer filament, or polymer in pellet form, is used as a stock material that is loaded to the machine. With the help of a motor, the polymer filament is driven to the liquefier to melt the polymer into its semi-liquid state as shown in Figure 1. Likewise, using stock in the form of pellets involves a lead screw attached to a motor to push the model material through the liquefier. The thermoplastic is extruded in a layer-by-layer fashion to create a 3D structure. Figure 1 also shows a support

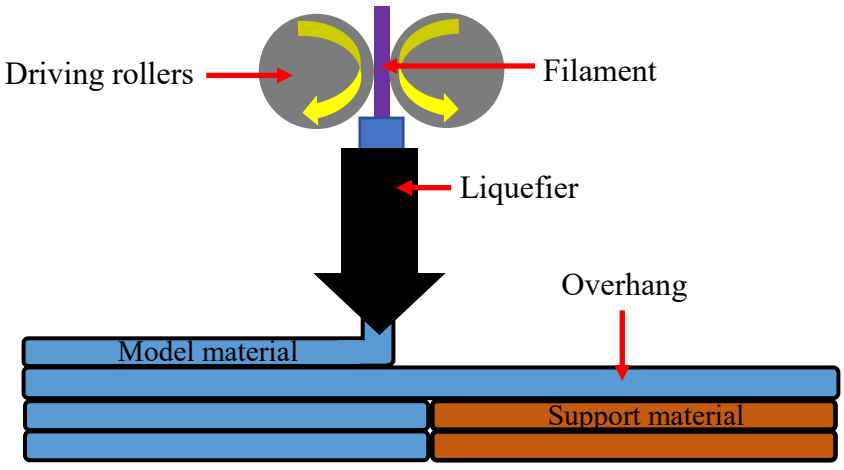

Figure 1 Material Extrusion process showing stock filament material (blue) and support material (brown)

material, typically of the same material in desktop 3D printers, to support overhangs of the model material. The general steps to obtain a finalized 3D printed part using material extrusion process are as follows: 1) a 3D part is drawn with the aid of a Computer-Aided Design (CAD) software, 2) the CAD model is converted into a file format named stereolithography (STL) that is traditionally used for 3D printing, 3) assign the printing job to the machine using the STL file, (in this step the user can manipulate the geometry's position, orientation, and scale), 4) set-up the machine prior to initializing the print (here the user sets the printing parameters for the machine), 5) build part, 6) remove the part from the AM machine, 7) post-processing (support material used is removed and the part is cleaned), and 8) the part is ready to be used (Gibson et al., 2015). This allows for rapid prototyping of a complex geometry that may not be possible to manufacture traditionally. When using the material extrusion process, one must consider how the part is placed within the slicer since the mechanical strength of a printed part is greatly dependent on the part orientation (Bagsik, 2010). Bagsik *et al.* showed mechanical strength results for test dog bones built in the X-, Y- and Z-direction following ASTM D638 (Tensile Test Methods for Plastics) specifications for Ultem*9085 (Polyetherimide). The maximum recorded stress was along the X-direction with an average tensile strength of 63MPa. The maximum tensile stress recorded for Y- and Z-direction were 46MPa and 41MPa, respectively.

2.1.1. Materials available in material extrusion:

Typical materials for material extrusion are thermoplastics such as acrylonitrile butadiene styrene (ABS), polycarbonate (PC), polylactic acid (PLA), and several grades of polyetherimide (PEI, also known by its tradename ULTEM) (Fischer, 2011). New methods have been investigated to improve the mechanical properties of blended thermoplastics with ceramics or metallic powders to obtain similar or better properties when compared to the fabrication of neat thermoplastics using injection molding (Dudek, 2013). For example, Siquieros *et al*. (2016) blended ABS with 75wt% styrene ethylene butylene styrene (SEBS) to generate a rubberized ABS printable filament that had a 98% increase in elongation (ASTM D638-10) compared to neat ABS.

Yang *et al. (*2017), proposed a mechanism that simultaneously deposited both semiliquid thermoplastics and continuous carbon fiber (CCF) through the same nozzle. A three-point bending test was performed following ISO 14125:1998 (Fibre-reinforced Plastic Composites – Determination of Flexural Properties) and showed a flexural strength of 127MPa compared to the printed ABS of a flexural strength of 80MPa. The inter-laminar shear strength was also tested using the ISO 14130:1998 (Fibre-reinforced Plastic Composites – Determination of Apparent Inter-laminar Shear Strength by Short-beam Method) and showed a shear strength value of 2.81MPa. Yang *et al.* expressed the shear strength results to be most vulnerable in carbon fiber reinforced thermoplastic composites (CFRTPC) when compared to injection molded ABS with a shear strength value of 24MPa. The last experiment used was ISO 527: 1997 (Plastics – Determination of tensile properties) standard to tests the tensile properties of the CFRTPC produced parts. The results for the ultimate tensile strength of the CFRTPC and injection molded ABS were 147MPa and 50MPa, respectively.

In contrast with the continuous fiber composites mentioned in this section, Ning *et al.* worked on the material deposition of a blend of neat ABS and carbon fiber powders of approximately 100-150μm at different contents (3wt%, 5wt%, 7.5wt%, 10wt%, and 15wt%) using a plastic extruder to create ABS/carbon fiber filament. Five experiments were performed to obtain the effects on tensile strength, Young's modulus, toughness, yield stress, ductility, and the effect on carbon fiber length on tensile properties. Standards ASTM D638-10 (Standard Test Method for Tensile Properties of Plastics) and ASTM D790-10 (Standard Test Methods for Flexural Properties of Unreinforced and Reinforced Plastics and Electrical Insulating Materials) were used to produce the test specimens. It was shown that the implementation of carbon fibers at 5wt% showed the best tensile strength results (42MPa). Specimens with 7.5wt% CF content showed the largest Young's modulus (2.5GPa). It was also easy to see that the increase in carbon fiber length lead to the increase of both tensile strength and Young's modulus. Finally, when comparing neat ABS fabricated parts to the 5wt% carbon reinforced ABS parts, Ning *et al*. showed that the flexural

stress, flexural modulus, and flexural toughness increased by 11.82%, 16.82%, and 21.86%, respectively.

To better aid with the material characterization of new materials, such as the ones mentioned in this section, the implementation of a continuous fiber—in this case copper wire—is discussed in chapter 3 using the proposed modular desktop 3D printer. This printer can help with the addition of a pellet extruder which may reduce cost of blending the thermoplastic with fibers to extrude a homogeneous filament. Basically, the modular desktop 3D printer allows for the implementation of a plastic pellet extruder mounted on the Z-stage of the 3D desktop system.

2.1.2. Pellet vs. Filament Extruders

Currently, the most popular type of polymer stock in material extrusion is filament in loose coil. To fabricate the filament, pelletized feedstock is processed using a screw extruder to provide thermoplastic feedstock ranging from 1.5-3mm (Turner *et al*., 2013). The filament travels down a liquefier with the help of a pinch roller mechanism with engraved teeth for better grip. As pressure increases within the liquefier, the material is heated and forced through a nozzle opening, commonly 200-500µm in diameter.

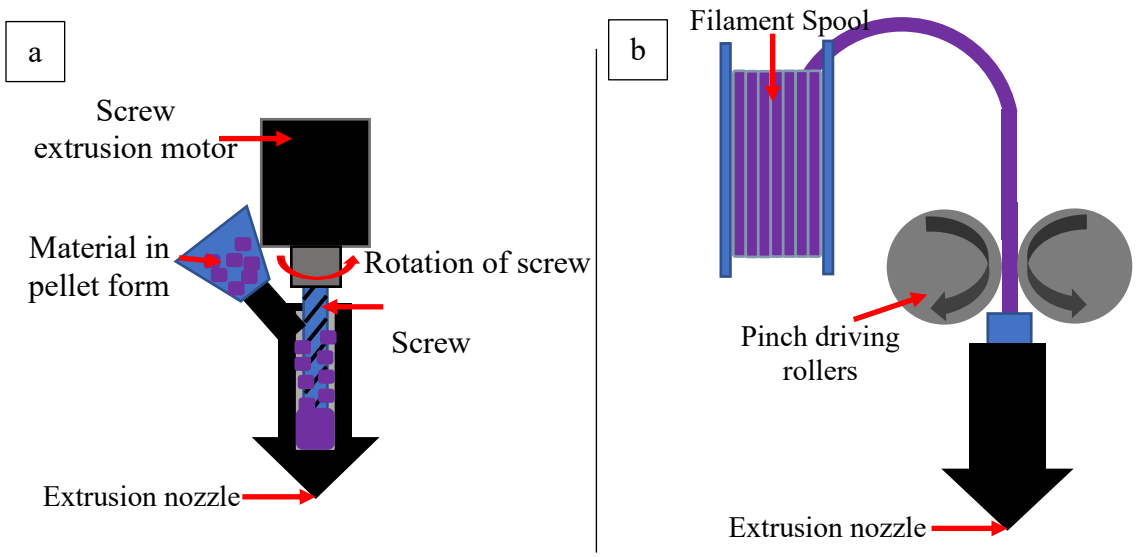

Figure 2 Process of material delivery and feeding to (a) pellet extruder and (b) filament extruder

Diagne *et al*. created a flow control model for dispensing polymer using a screw extrusion. This type of extrusion does not require filament feedstock material, therefore, allowing for easier printing of recycled materials. However, a deposition hysteresis is usual in pellet extruders, therefore, a predictor feedback controller based on material rheology and heat transfer was used to control the flow when using a screw extrusion. Figure 2 shows the delivery and feeding of the material in two different types of extruding mechanisms.

Currently, two types of filament-based extruders are being used in printers to extrude material. The two types are Direct Drive extruder and Bowden extruders as described by the website "matterhackers.com". The main difference between the two extruders is the material feed/delivery method to the hot end. The Direct Drive mechanism allows for a shorter distance between the driving mechanism and the nozzle. This aids by providing responsiveness (hysteresis or lag) of the material deposition when compared to Bowden extruders as said by Landry from matterhackers. A major strength of a Direct Drive extruder, is the ability to print flexible materials (e.g. Ninjaflex) due to its direct guidance, hence, not allowing the flexible filament to buckle, jam, and/or fail.

Bowden extruders on the other hand have greater distances between the driving mechanism and the hot end. The driving mechanism is externally mounted which feeds the filament through a Teflon tube and into the hot end. Since most printers have a dynamic hot end and a stationary print bed, a Bowden extruder is recommended to allow for a faster and more accurate print due to the absence of the driving mechanism mounted on the axis. Therefore, the Bowden extruders significantly decrease the weight of the axis that the hot end is carrying.

2.1.3. Control algorithms for extrusion Axis synchronization

It is important to discuss the method for the X- and Y-axis synchronization with the rate of extrusion, noted as E-axis. To have a better idea of the deposition rate of material, Benilli *et al.* (2004) expressed an equation for the linear feed velocity using pinch rollers:

$$v = \frac{Q}{WH} \qquad (1)$$

where:

v = velocity of the filament

Q = volumetric flow rate of material from the nozzle

W = desired road width

H = layer thickness

Coupling equation (1) with the feed velocity, assuming no slip, can be obtained by:

$$v = \omega_r R_r \qquad (2)$$

where:

ω_r = angular velocity of the pinch rollers

R_r = radius of the rollers

2.2. TYPES OF DESKTOP 3D PRINTERS

A review on desktop systems with a price range of 200-5000$ US-dollars was performed. A 3D printing service website known as 3dhubs.com compares the current desktop systems based

on process, price, build size, and user ratings. Material extrusion 3D printers will only be compared since this is the focus of this manuscript.

Typical desktop systems are shown in Table 2 along with their respective built volume and user ratings. Typical hardware from the listed 3D printers include stepper motors, toothed timing belts for XY-axis movements, lead screws for Z-axis, build platform (typically made of glass, aluminum, medium density fiberboard), controller, and power supply (Jones *et al*., 2011). Understanding the current hardware allowed for considerations during the design and development process of the proposed modular desktop 3D printer.

Table 2 Popular 3D systems in 2018 according to 3dhubs.com

3D printer	Build size (cm x cm x cm)	Price US dollars
Original Prusa i3 MK2S	25 x 20 x 21	726.00
CraftBot	25 x 20 20	999.00
Raise3D N2	30.48 x 30.48 x 30.48	2,799.00
Ultimaker 3 Extended	21.5 x 30 x 21.5	4,295.00
LulzBot Taz 6	15.2 x 15.8 x 15.2	2,500.00

2.3. RANKING MODEL

A NIST additive manufacturing test artifact was proposed to standardize printer characterization (Moyland *et al.,* 2012). Moylan *et al.* described the need for the test artifact as many machines are not capable of obtaining feedback from sensors such as thermocouples and motor velocity and position sensors of the machine due to the extreme environments that the components are exposed to. This limits the amount of instrumentation (i.e. sensors) that can be implemented, therefore, limiting the in-situ monitoring. Moylan *et al.* said that a machine error directly contributes to the fabrication error of a 3D printed part. Previous tests artifacts were evaluated to obtain the NIST test artifact shown in Figure 3.

The following lists key features used to characterize 3D printers formed by Moylan:

- Straight features

- Parallel or perpendicular features
- Circular or arced features
- Concentric circles or arcs
- Fine features
- 3D or freeform features
- Holes and bosses
- Multiple planes
- Location and orientation
- Geometric errors of mirror positioning axes
- Geometric errors of build platform
- Alignment errors between axes
- Errors in beam size

Prior to building, the test artifact must be positioned in the center of the build platform with the 4 pins aligned along the X- and Y-axis. The part is 101000mm^3 in volume and 17mm tall. A smaller modified version (Perez *et al.*, 2013) of the test artifact proposed by Moylan will be used to characterize the proposed modular desktop 3D printer.

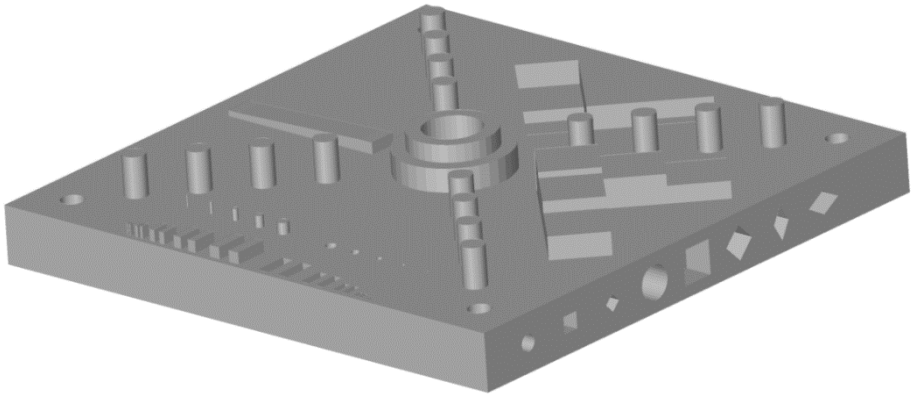

Figure 3 Moylan *et al.* NIST AM test artifact

2.4. HEAT TRANSFER OF BUILD PLATFORM

Most current 3D printers are equipped with heated beds to avoid part warping due to shrinking of the deposited thermoplastic. If the polymer is exposed to different temperatures, then the part is very likely to fail due to adhesion or warpage. Typically, to avoid warpage on a 3D printed part the build platform temperature is set to a value close to the material's glass transition temperature. For example, ABS has a glass transition (TG) temperature roughly at 110ºC and a thermal expansion (CTE) value of ~90µm/m-K when compared to PLA that has a TG temperature at 60ºC and a CTE value of 68µm/m-K according to "cosineadditive.com". To quantify the heat transfer of a horizontal plate, an analysis of natural convection was performed to the build platform. Cengel *et al.* showed that the heat transfer coefficient (h) can be obtained by using the following equations:

$$Nu = \frac{hL_c}{k} \qquad (3)$$

where:

Nu= Nusselt number

L_c= Characteristic length

k= thermal conductivity of air

To account for the natural convection, the Rayleigh number accounts for the buoyancy forces, thermal diffusivities, and momentum diffusivities expressed as:

$$Ra_L = \frac{g\beta(T_S - T_\infty){L_c}^3}{\nu^2} Pr \qquad (4)$$

where:

g= acceleration of gravity

β= volume expansion coefficient

k= thermal conductivity

Pr= Prandtl number

The Rayleigh number affects the Nusselt number *Nu* for a plate that is insulated from the bottom and exposed to air on the top surface. The heat transfer coefficient obtained using this analysis was used to model the temperature distribution when a 200W heat source is placed inside the build platform. Thermal experiments to validate the output of the heat transfer analysis are expressed in Chapter 4.

2.5. ULTRASONIC STRENGTHENING EFFECT ON 3D PRINTED POLYMERS

As mentioned in the previous section, material extruded parts have a weak mechanical performance if the direction of stress is perpendicular to the bead direction. Therefore, efforts on improving the mechanical performance of material extrusion printed parts have been of great interest. Guiwei *et al*. (2018) used ultrasonic vibrations to increase the mechanical performance in acrylonitrile butadiene styrene (ABS) samples. Guiwei *et al.* showed the energy (Q) input that a 3D printed sample experienced from the high vibrations of an ultrasonic horn. Equation (5) is expressed as:

$$Q = 4ASFkft \qquad (5)$$

where:

A = amplitude

S = contact area between ultrasonic horn and 3D printed specimen

F = strengthening pressure

k = friction coefficient

f = frequency

t = ultrasonic strengthening time

Tensile tests were performed on five ultrasonic strengthened samples to compare with five unstrengthen samples. Ultrasonic strength time of exposure and the pressure applied to the 3D printed samples were varied for the experiments. Ultrasonic strengthened samples showed an

increase in tensile strength of 11.3% and an increase in the Young's modulus of 16.7% when compared to the untreated 3D printed specimens. The fracture characteristics were also observed using a digital microscope to understand the effect on quality due to the ultrasonic post processing. It was noted by Guiwei *et al.* that if the energy input by the ultrasonic vibrations is too large, the surface in contact with the horn may be severely damage, however, if the correct time and pressure (0.45 sec at 3.5 kg/cm^2) is applied, the surface becomes smoother and the mechanical properties increase due to the fusion between beads and layers.

2.6. 3D PRINTED ELECTRONICS

Espalin *et al.* (2014) made a comparison for creating circuitry via direct print technologies using vat-polymerization process, direct print technologies with material extrusion process, and embedding of solid copper wire onto material extruded parts. To generate the material extruded parts, a system referred to as the multi^{3D} system was used. This system included two material extrusion 3D printers, a CNC for micromachining, and an apparatus that submerged (embedded) solid copper wire onto a thermoplastic substrate. A rectangular 3D printed CubeSat module was additively manufactured using both stereolithography (resolution of ~75μm diameter) and material extrusion (resolution of ≥ ~254μm diameter). The module consisted of a two-axis gyroscope and used IIC communication that continuously transferred data every minute when tested in low Earth orbit. Additionally, a serpentine design conductor was printed on the rear of the CubeSat module to measure resistance based on applying different voltage when exposed to the harsh environment of space.

The material extrusion CubeSat was fabricated using the multi^{3D} system, a LabVIEW controlled system that used a sliding platform to translate the build platform to different compartments. Two compartments were used for two material extrusion printers, and the third compartment housed the following technologies: micromachining, component placement, ink

dispensing, and wire embedding. Two distinct methods of manufacturing the CubeSat's interconnections were investigated: conductive inks and solid copper wire traces. Both methods were manufactured via material extrusion using the multi^{3D} system. First, a comparison of printing an ULTEM 9085 CubeSat with interconnections versus printing the component cavities using the printer's resolution was performed. On the other hand, an ULTEM 9085 CubeSat blank substrate was printed and both the component cavities and conductive ink interconnection channels were machined using feeds and speeds for polycarbonate. ULTEM 9085 was chosen as a baseline material due to its similar electrical properties when compared to Kapton and FR-4 materials. Comparing ULTEM 9085 with FR-4, an epoxy used for printing circuit boards, a volume resistivity of 1.0E+14 – 6.0E+13Ωcm was seen on the ULTEM 9085 material and a volume resistivity of 5.0E+12Ωcm was noted for the FR-4 epoxy. A dielectric constant of 3.5 for ULTEM 9085 compared to 4.6 for FR-4, and a dissipation factor of 0.0026 for ULTEM 9085 compared to 0.015 FR-4 was seen.

Direct print technology

Direct print technology is a method that uses material extrusion combined with micro-dispensing (Rojas *et al.*, 2017). This method allows for the deposition of conductive inks, such as Dupont Ink CB028 Silver and Dupont Ink CB500 Copper, onto channels that represent electrical traces. Espalin *et al.* reported on the FDM fabricated CubeSat with interconnections from Dupont Ink CB028 Silver ink dispensed into channels having the following dimensions: 127-μm thick and 100-μm wide. The interconnection channels were machined to a depth of 0.127μm, which is half of the layer thickness, and parallel traces were spaced 254μm apart. The resolution of the CNC router was 5.08μm with a repeatability of 25.4 μm and end mills having diameters of 3.18, 1.59, 1.27, 0.51, and 0.41mm were used. After machining, conductive ink (model 1660, Ercon Inc.,

Wareham, MA) was deposited inside the channels using a precision dispensing system attached to the third compartment of the multi^{3D} system. Components were inserted manually, and the CubeSat module was placed in an oven at 60ºC for 60 minutes to cure the conductive ink.

The micro-machined ULTEM 9085 substrate demonstrated high quality component cavities and interconnection channels having a width of 506±4µm. Material extrusion without micromachining post-processing was not able to produce component pin cavities, interconnection channels, nor pin-interconnect junctions. The total time of machining the top and bottom surfaces of the CubeSat was 11min. Testing of inks using material extrusion required high densities and smooth channels to avoid spreading to different electrical traces and creating a short circuit. It was noted that a -38.1 µm raster-to-raster air gap and a cutting depth of 127 µm, the conductive ink did not spread to different traces. Therefore, the CubeSat was fabricated with the described parameters. Obtaining high detailed features using material extrusion to accommodate electronics such as the 144-pin TQFP package, that requires 450-µm openings and 200-µm separation fins, was challenging to machine due to the small features.

2.7. Wires

Espalin *et al.* also embedded solid copper wire via ultrasonic energy (20kHz, 500W power supply) into an ULTEM 9085 polymer to generate interconnections for the CubeSat module. Since wire embedding was at an early stage, it was not possible to create complicated geometries as the CubeSat. A simpler pattern of an antenna was manufactured by embedding copper wire into a polycarbonate substrate. Embedding of different copper wire gauge (40, 32, and 28AWG) was also tested on a PC and ULTEM 9085 substrate. Espalin *et al.* noticed a relation of heat-affected zones which increased with larger wire diameters. A need for processing parameters such as ultrasonic

amplitude, pressure applied during embedding, substrate material, surface roughness, and traversing speed is believed to greatly affect the embedding quality.

Wicker *et al*. (2016) emphasized "embedding solid conductors within polymer substrates using ultrasonic or thermal energy to provide high performance electrical interconnect". This states that solid copper wire is used for high current demanding electronics (i.e. 5A for power transmission) such as motors, resistors, actuators, etc. without affecting the polymer surrounding the conductors. It is obvious to see that copper solid conductors are commonly used for high power demanding electronics, therefore, it is a viable approach to apply the same concept on the modular desktop 3D printer.

Embedding solid copper wire with a compact 3D system is the aim of this project. The approach is to create a compact version of the multi^{3D} system to easily generate 3D printed electronics similar to PCBs to produce customized prototypes faster when compared to traditional manufactured PCBs. With the aid of a G-code post-processor (Bailey *et al.*, 2016) and the implementation of the items mentioned in this literature review helped on the development and fabrication of a hybrid modular desktop 3D printer with wire embedding.

CHAPTER 3

MODULAR DESKTOP 3D PRINTER WITH WIRE EMBEDDING

3. DESIGN OF 3D PRINTER

3.1. Hardware

A major design requirement was to fabricate and develop the modular desktop 3D printer with "off-the-shelf" parts. This allowed for easy replacement of damaged components due to wear or accidental collisions. Another requirement was to design for modularity to implement additional tools (e.g. wire embedding, machining), additional motors for path dependent tools, additional degrees of freedom, cameras for machine vision, etc. The following three sections will describe the process used to develop and fabricate the 3D printing machine.

3.1.1. Design

Figure 4 shows the computer aided design (CAD) version of the modular desktop 3D printer designed using SOLIDWORKS. The system uses a three-axis XYZ Cartesian gantry driven

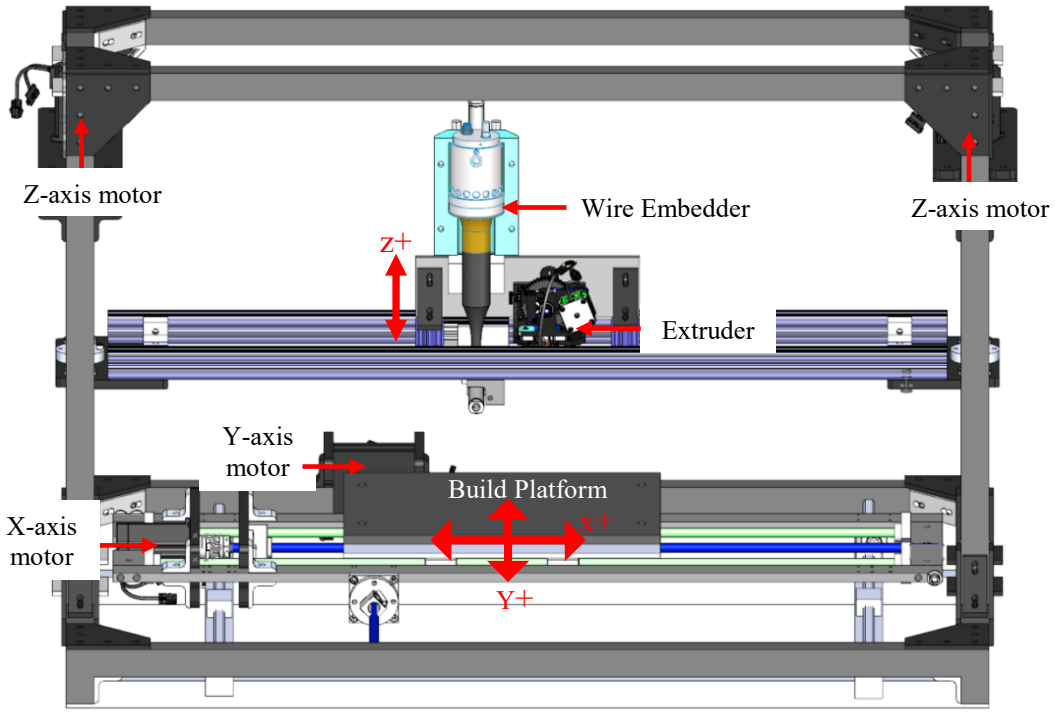

Figure 4 Modular desktop 3D printer 3-axis gantry

by lead screws (XY-axis travel distance of 25.4 mm/revolution and Z-axis travel distance of 2.54 mm/revolution) and a corresponding travel nut attached to each axis. The frame of the printer was made of AL 6105-T5 extrusion bars (38.1 x 38.1 mm (1.5 x 1.5 in.)) with T-slotted profiles to provide structural support and easy assembly and disassembly of the system. The extrusion design allows for easy implementation of additional structural support if needed.

The XY motion is delivered to the build platform and the tools are translated along the Z-axis. As mentioned in Section 2.1, most desktop 3D printers consist of toothed timing belts for XY-axis movements and lead screws for motion along the Z-axis. Also, during printing most desktop 3D printers translate the tool along the X-axis while moving the platform along the Y-axis. During rapid, non-depositing movements, the tool is translated along the Z-axis. A common printer that employs this coordination is the LulzBot Taz 6 (Aleph Objects, Loveland, CO). The proposed system (modular desktop 3D printer) was designed to translate the build platform along the XY-axis and translate the tool up and down along the Z-axis to allow for implementation of tools with greater payload (maximum payload is described in the XYZ-axis load analysis) without affecting print speed and quality due to the large momentum of the tools.

XYZ axes load analysis

The Z-axis has two 38.1mm (1.5in) aluminum extrusions that holds tools such as the pneumatic actuator used to offset the wire embedding sonotrode up and down to allow for multiple processes to happen without manually interchanging tools. Tools can be completely removed if needed to accommodate larger tools (e.g. pellet extruder, foil embedding, spindle for machining, and a camera for machine vision). Currently, the system setup has been configured to easily accept wire embedding, machining, and material extrusion. Two NEMA 23 stepper motors were installed to translate the tool carriage along the Z-axis, however, it was critical that the motors perform adequately. Force analysis was performed on the Z-Axis to size the motors to lift a demanding weight of ~68 kg (~150lbs) (maximum anticipated weight of tools) at the middle of the axis as shown in Figure 5:

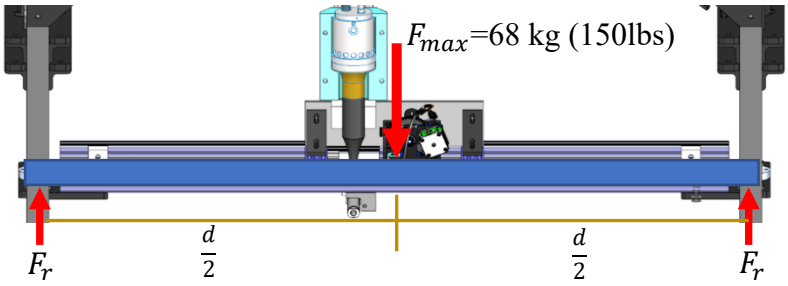

Figure 5 Force analysis of Z-axis to quantify the maximum payload

Applying static equilibrium of force and moment analysis shows the reaction forces from the weight of the tool as follows:

$$\uparrow + \sum F_z = 0: \qquad 2F_r = F_{max} = 68kg\ (150lbs) \qquad (6)$$

The following formula obtained by "Shigley's mechanical engineering design" was used to obtain the torque *Tr* when raising the Z-axis:

$$T_r = \frac{F d_m}{2}\left(\frac{l + \pi f d_m \sec\alpha}{\pi d_m - f l \sec\alpha}\right) \qquad (7)$$

where:

F =reaction force in the nut

d_m = mean diameter of the lead screw

p = pitch of the screw

α = thread angle

f = friction coefficient

l = lead (pitch * number of engaged threads)

As mention previously, two ½”-10 ACME 304 stainless steel screws with a travel distance of 2.54mm (0.1in) having an accuracy of ~±0.75mm/m (±0.009in/ft), listed by manufacturer, were chosen to translate the Z-axis supported by two ACME nuts. The ½”-10 ACME externally threaded nuts, composed of 673 Bronze, connected to a threaded flange that connects to an aluminum plate as shown in Figure 6. Two guide rods with bearings, shown in green, keep the axis aligned by constraining the motion in all direction except along Z axis.

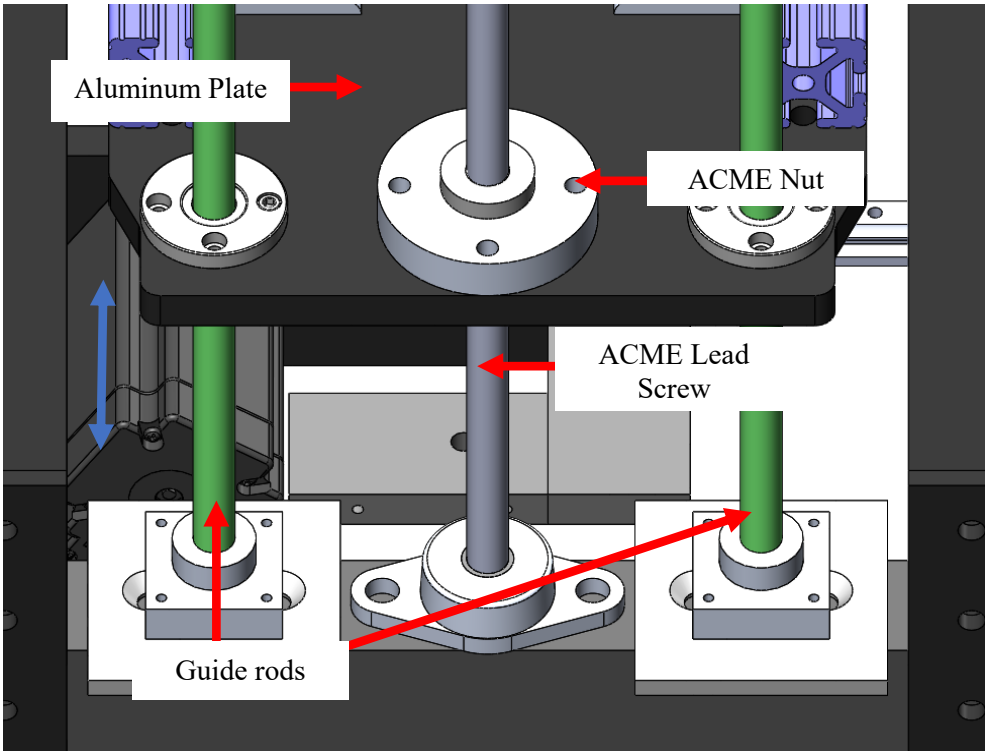

Figure 6 Configuration of components used for motion along the Z-Axis

Substituting the lead screw and nut parameters into equation 7 results in a torque of 0.5N-mm. Therefore, a NEMA 23 stepper motor with a static torque of 2.4N-m and encoder resolution of 1000 pulses per revolution was chosen from Parker Hannifin (Cleveland, OH) motor manufacturer. The chosen motor, NEMA 23 stepper motor (part number: ECLD-4DC-PC603A) allows for a maximum payload of 86 kg (190lbs) when a load is at the center of the Z-axis according to the analysis from equation 7.

Build platform

Two NEMA 23 stepper motors were chosen to provide motion to the build platform with the help of two ½"-8 ACME 1018 Carbon Steel lead screws and their corresponding ½"-8 ACME Bronze nut. However, to quantify the payload of the build platform, a static Finite Element Analysis (FEA) was performed to understand the strain energy distribution when printing 2kg of ABS. A simplified version of the CAD model was obtained to perform the FEA analysis and the following boundary conditions were applied as shown in Figure 7:

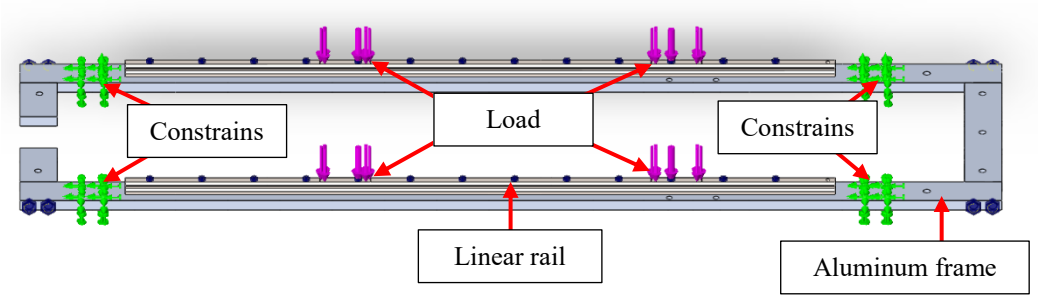

Figure 7 Simplified X-Axis gantry used for FEA analysis

The purple arrows in Figure 7 represents the load applied to the linear rails and the green components indicate the fixtures/constrains of the assembly. Contacts surfaces were defined between the aluminum plates and linear rails. Then, the linear rails were attached to the 6061-aluminum frame with the help of 13 8-36 machine screws on each rail. Finally, 8 3/8-16 screws were used to couple the aluminum frame with a preload of 3Nm. The total weight of the assumed 2kg of ABS and the build platform combined added up to 9kg (~20lbs). The FEA analysis was performed using SolidWorks static study using a standard mesh of 5mm in size with a tolerance of 0.25mm. Figure 8 shows the meshed components and the results from the study. A maximum von Mises stress of 235.9MPa at the alloy steel rail was calculated, which was below the material's yield strength of 655MPa. A maximum strain of 1.8e-3 was calculated at the interface between the aluminum plate and alloy steel rails.

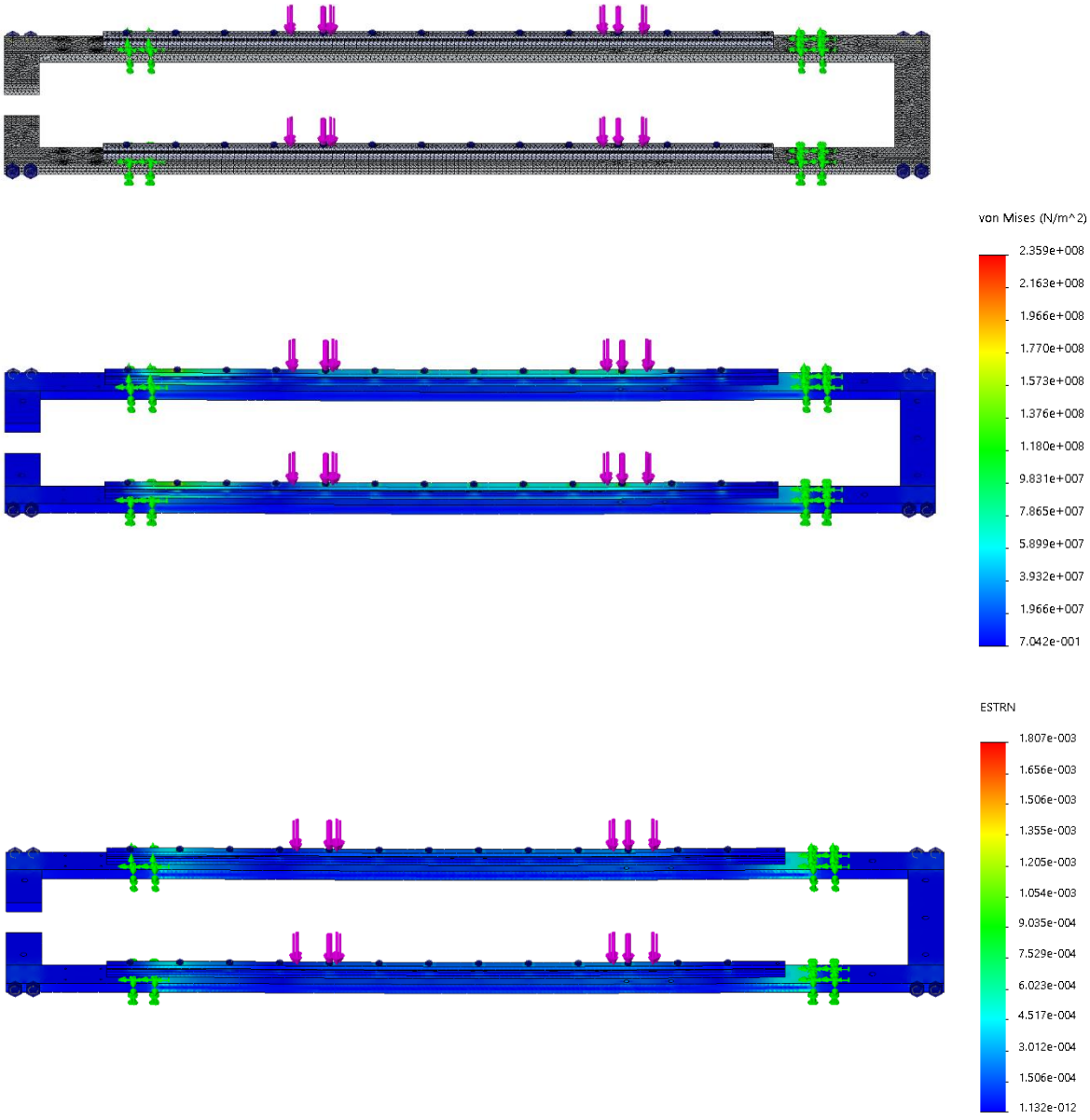

Figure 8 Finite element analysis of X-axis and results (a) meshed components (b) Von misses stress when 9kg (20lbs) were applied (c) strain caused by the 9 kg (20lbs)

An aluminum build platform was chosen for its rigidity over a glass bed. It is believed that the glass could potentially shatter with the vibrations provided by the ultrasonic horn during wire embedding. A spring loaded leveling mechanism was introduced, however, to reduce vibrations from the system, the build platform was completely constraint with aluminum spacers and the springs were removed. Four 200W cartridge heaters were installed in the corners of the build platform to provide a symmetric temperature distribution and a thermocouple type K sensor was

placed next to a heater to control the temperature. A temperature analysis will be discussed in the methodology chapter.

3.1.2. Construction

Filament-fed material extrusion

Another key requirement of the 3D system was to print using filament of both typical material and high temperature material for future projects. Table 3 shows common extruders used for open source desktop 3D printers. The construction of this table allowed for a visual comparison

Table 3 Extruders considered for the characterization of the modular desktop 3D printer

1. 	2. 	3. 
• Grade 5 Titanium Heat Break (isolates heater and cooling block and provides a more defined melt zone) • Aluminum Cooling Block • Aluminum Heater Block • Brass Plated Wear Resistant MK8 0.4 mm Nozzle • Used for high temperature materials (~315°C)	• High-purity aviation aluminum • Straight through throat, allows direct access to the nozzle which makes feeding more smoothly to reduce clogging. • Maximum temperature should not be over 260°C, can go higher but will cause Teflon inside to melt and clog.	• Maximum temperature should not be over 260°C, can go higher but will cause Teflon inside to melt and clog. • Includes direct driving mechanism.
4. 	5. 	6. 
• Multi-color extruder hot end • 1.75 mm • 0.4 mm Nozzle • Color switching waiting distance is less than 45 mm • Maximum temperature should not be over 260°C, can go higher but will cause Teflon inside to melt and clog.	• Capable of printing high temperature point plastics such as nylon and polycarbonate • Wiring insulation using high temperature Teflon/PTFE • Metal Design • Silicone heat protection sock	• MACHINED (Heatsink, V6 Heartbreak, v6 Heater Block, v6, 0.4 mm Nozzle) • PLASTIC (Titan Body, Idler Lever, 1.75 mm Filament Guide, 2.85 mm Filament Guide) • Includes driving mechanism.

of extruders that met the system requirement based on the comments of users and manufacturer specifications.

The third extruder was chosen from the table above for its direct driving ability. According to comments from users within the open source additive manufacturing community, this extruder provides faster extrusion responsiveness due to its shorter distance between the driving mechanism and the hot end. The chosen extruder will not extrude high temperature materials (≥ 300ºC) since it will melt the Teflon coating inside the liquefier. Also, this direct drive extruder will allow to better characterize the machine since it eliminated variables generated by material extrusion responsiveness and lag.

Wire embedding

A CPX 500 ultrasonic homogenizer (Cole-Parmer Instruments, Illinois, USA) with a power of 500Watts and a frequency of 20KHz was used as the method for embedding solid wire (32-24AWG) onto a plastic substrate. A pneumatic linear slide was installed to carry the ultrasonic horn and allow for multiple processes to happen without having to reconfigure the machine by

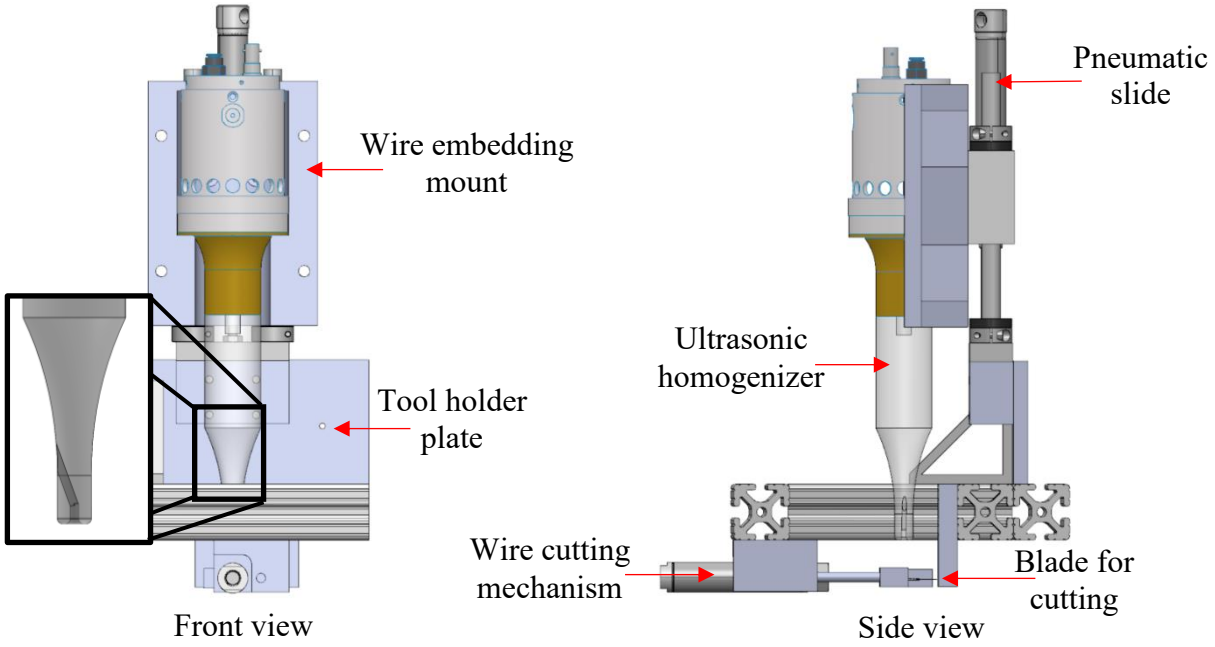

Figure 9 CAD version of wire embedding tool

manually exchanging tools. A plastic mount was designed and printed to constrain the horn by tightening four bolts and allow most of the energy transfer to the plastic substrate when embedding. Finally, to completely automate the wire embedding process, a wire cutting mechanism device was designed and implemented. To cut the wire a pneumatic piston was introduced to push a standard rectangular blade against an aluminum plate and shear the wire. Figure 9 shows a CAD version of the wire embedding assembly. The ultrasonic horn is 12in tall and contains a 0.405mm diameter where the wire exits is also shown in Figure 9.

A total of 12 aluminum plates were machined using a CNC machine to construct the 3D printer. While the requirement was to use "off-the-shelf" components, a few plates had to be designed and machined to allow the implementation of motors, tools, linear rails, and the build platform.

3.1.3 Assembly

The 3D printer was assembled in an estimated time of 2hrs using typical hardware found in a toolbox such as a standard allen key set, phillips screw driver and crescent wrench. The following lists machine specifications:

- A maximum build volume of 17inx13inx18in may utilized for both printing and wire embedding
- The modular desktop 3D printer has dimensions of 4.12ft x 2.93ft x 2.5ft (excluding the desk where the system rests)
- The system has an estimated weight of ~113 kg (250lbs) when configured to wire embedding and material extrusion
- A power input of 120VAC/20A is required to operate the machine
- Compressed air within the range of ~278 to 552 kPa (40psi to 80psi) is required to fully operate the machine

Figure 10 shows the assembled system with wire embedding and material extrusion configuration.

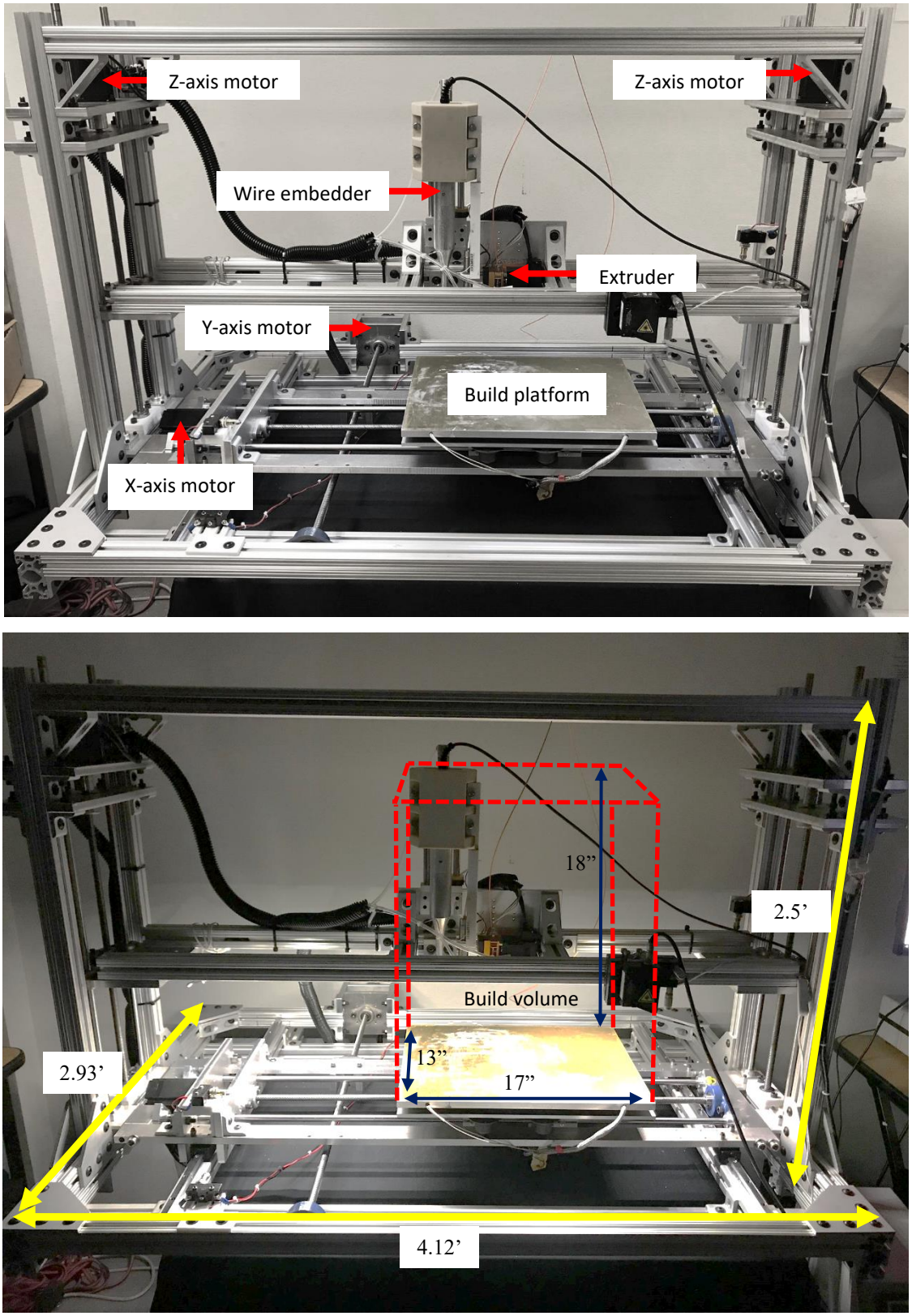

Figure 10 Modular Desktop 3D Printer with Wire Embedding Tool

3.2 Firmware

Along with the modularity of this system, an industry grade Programmable Logic Controller (PLC) (mainly used for CNC operations) was chosen to add both reliability and feedback to the machine. A Parker Automation Controller (PAC) (Parker Hannifin, OH) was chosen due to its modularity and low price when compared to Yaskawa and Delta Tau PLC and motor drivers. Using a PLC and not a low power open source controller (e.g. Rambo 1.3l) allows the researcher to implement and reconfigure the logic and hardware to the system.

The following Parker Automation Controller was purchased along with the motor drivers and analog modules:

- PAC Model number: PAC320-CWE21-3A
- Motor drivers for NEMA 23 stepper motors: ECLD-4DC-PC603A
- Motor drivers for NEMA 17 stepper motors: ECLD-4DC-PC173A
- Thermocouple Module: PACIO-443-06
- Analog Module: PACIO-441-01

Figure 11 shows the basics of the controller and how the system was divided. A user communicates to the controller via a human machine interference (HMI). The PAC receives the instructions obtained from the user and interprets the G-code and checks for speeds and accelerations that may damage the motors. The interpreter then outputs motion for the XYZE axes if no errors were found. One digital and one analog module was used to control the inputs and outputs of the machine used for limit switches, proximity sensors, air valves, relays, temperature control, and emergency stop button. Also, digital output signals of 24V controls external devices such as the wire embedder to switch on or off.

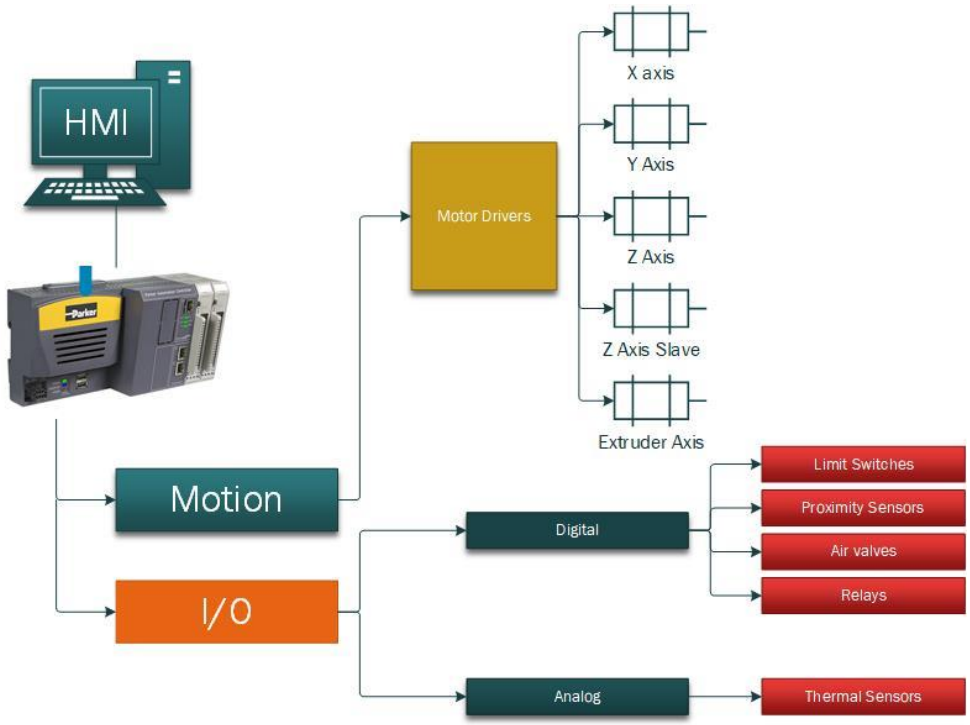

Figure 11: Controller Topology

It was important to understand the PLC programmable environment language to implement the material extrusion process in a CNC oriented PLC. A walkthrough written by Halimic 2016, was used to create a CNC application that used functions such as a G-code interpolator, axis control, and transformation of inverse kinematics. The walkthrough showed the main structure of a PLC continuous function chart used for a CNC. It also showed how to load and execute G-code to achieve motion.

A flow chart summarizes the continuous function block used in the 3D printer to execute a G-code on the printer (Figure12). To execute a G-code, the user defines the temperatures via HMI in which the temperature control function block activates to maintain the set temperature. Notice that the temperature function block does not contain any type of proportional, integral, nor derivative gain (PID) parameters. Therefore, currently functioning as an ON/OFF switch to supply current to the heaters with the help of a 24VDC solid state relay.

To zero the XYZE axes, the homing sequence is executed in which the motor moves to the negative position until a limit switch activates. When the limit switches become true, the motor

stops and sets a value of zero to its current position. The G-code is then executed, read and checked by the interpreter. If the accelerations and speeds do not exceed the motor's abilities, motion will begin, otherwise, the interpreter will activate the emergency stop function which completely stops any current sequence in the controller. M-commands are programed sequences that enables outputs from the machine to turn on external equipment. In the case of the 3D printer, the wire embedder may be controlled via M-commands to switch on when needed.

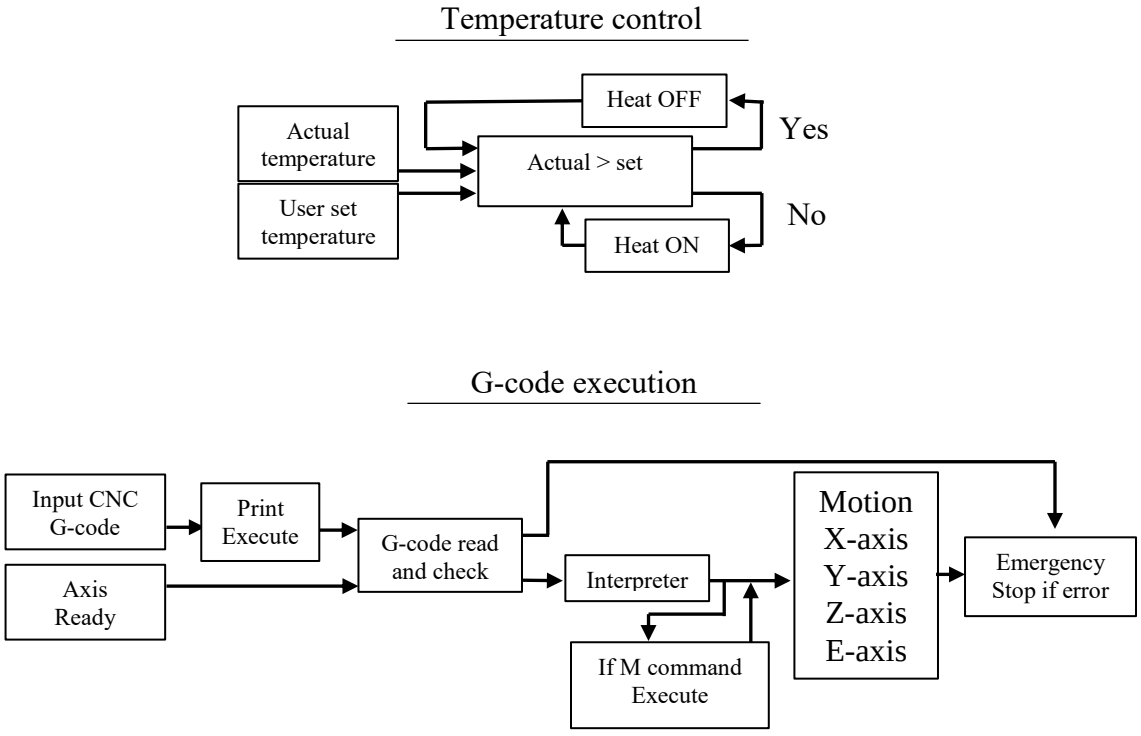

Figure 12 Flow chart of continuous function block

An HMI (Human Machine Interaction) was developed using the Parker Automation Manager PAM to turn on, jog, home and zero the axis. G-code is uploaded to the PLC via the PAM software and the G-code is executed by the user in the HMI. Also, the HMI contains the heating controls for both the nozzle and bed and displays the current temperature of the thermocouple sensors. A computer was connected via Ethernet using the following IP address 192.168.10.51 and

the subnet mask 255.255.0.0. Figure 13 shows the HMI displayed by the computer used to control the 3D printer.

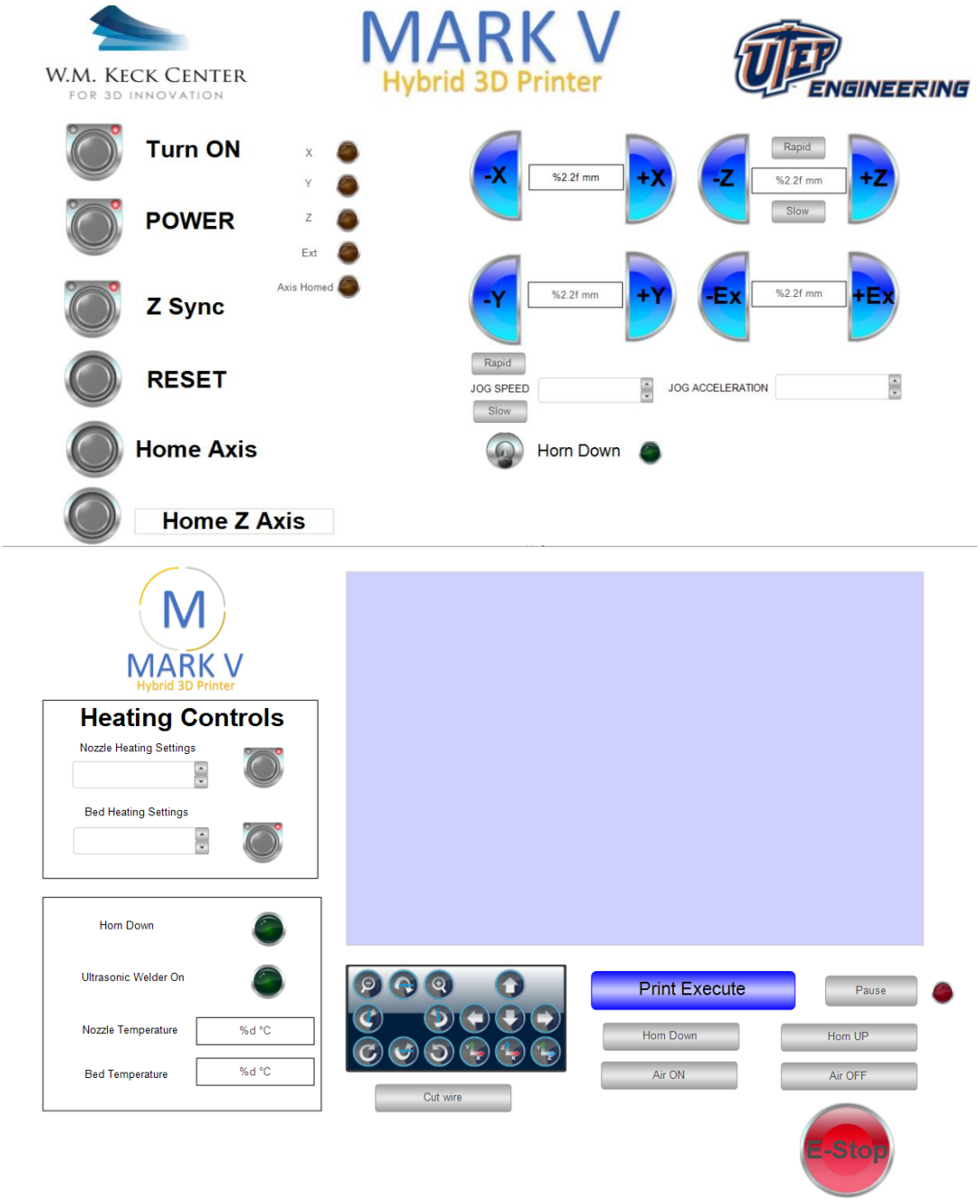

Figure 13 Human machine interaction of the modular 3D system

CHAPTER 4:

CHARACTERIZATION AND EXPERIMENTATION OF THE MODULAR 3D PRINTER

To understand the dimensional accuracy of the XYZ axes, a test was performed to quantify the repeatability of the X-, Y-, and Z-axis in terms of motion. The extruder gear ratio was calibrated to print a part or model (referred to as a "ranking model" since the designer of the part originally used this model to evaluate and rank desktop printers (Perez *et al.*, 2013)) and was compared to a Fortus 400mc (Stratasys, Eden Prairie, MN) production grade 3D printer. The following formulas were used to calculate the percent error and standard deviation of then following experiments.

Equation 8 shows the method for calculating percent error:

$$Percent\ error\ (\%) = \left|\frac{V_{true} - V_{observed}}{V_{true}}\right| * 100 \quad (8)$$

where:

V_{true} = True value

$V_{observed}$ = Observed value

Equation 9 shows the method for calculating standard deviation (*s*):

$$s = \sqrt{\frac{1}{N-1}\sum_{i=1}^{N}(x_i - \bar{x})^2} \quad (9)$$

where:

N = number of data points in sample

$\bar{x}$= mean of the data set

x_i= value in the data set

4.1.Test 1. Laser Displacement Sensor Repeatability

The objective of this experiment was to calibrate the sensor and understand the laser displacement sensor (LDS) variance when taking measurements. A Microtrak Laser displacement system 7000 (NY) and a two-axis leveling mechanism was attached to the printer as shown in Figure 14. The following methodology and procedures were followed to calibrate the LDS.

1. Zero the Laser Displacement sensor (LDS) to the build platform of the printer
2. Place a 2.54mm (0.1 in.) rectangular gauge block under the laser as show in the Figure 14A
3. The gauge block is 0.1in (2.54mm) in thickness; therefore, the laser should display the gauge width value and interpretation should consider the laser resolution of ±2.54µm
4. If the LDS did not display the correct values, the knobs on the leveling mechanism should be used until the correct value is displayed by the LDS. This ensured that the LDS is normal to the gauge block
5. Remove gauge block from LDS
6. Repeat steps 1-6

If the LDS displays the correct measurement of the gauge block, proceed with the following steps to obtain the laser's repeatability:

1. Zero the LDS to the build platform of the printer
2. Place a 0.1in (2.54mm) rectangular gauge block under the laser as show in the Figure 14A
3. Record the value displayed by the LDS
4. Repeat steps 1-3 ten times to obtain a standard deviation

5. Repeat steps 1-4 for a 0.2in (5.08mm) rectangular gauge block

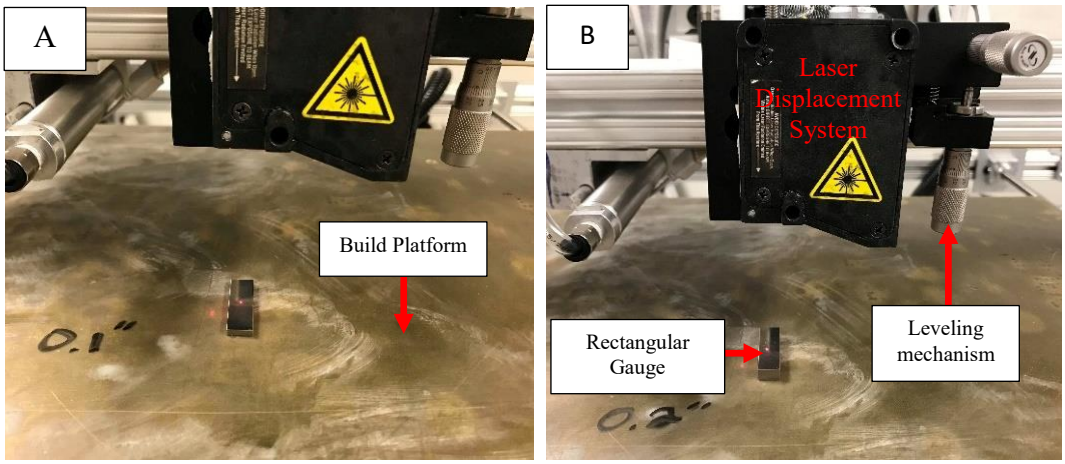

Figure 14 Laser Displacement System Calibration

4.1.1. Test 2. XYZ-axis repeatability

The following tests were performed to understand the repeatability of the XYZ axes and translate the variance of the system to part dimensional accuracy. A laser displacement sensor was fixed to the Z axis of the 3D printer as shown in Figure 15. The following G-Code was used to translate the axis up and down:

N0 G1 F8 E800 E-800

{N10 G1 Z0

N20 G4 T8

N30 G1 Z-2

N40 G4 T8**}** Repeat 10 times

The first line (N0) of the G-code shown above defines the speed of the Z-axis (F8mm/min) and its acceleration/deceleration (E±800mm/min^2). A time delay of eight seconds was implemented to record the LDS displayed value using a dwell G-Code function (G4 T8secs). The Z-axis travels downward until reaching 2mm with the "G1 Z-2" line.

Figure 15 also shows the test setup of the repeatability tests for the XY-axis. The following G-codes were executed for this test in a similar way:

X-Axis Repeatability G-code	Y-Axis Repeatability G-code
N0 G1 F8 E800 E-800	N0 G1 F8 E800 E-800
{N10 G1 X0	**{**N10 G1 Y0
N20 G4 T8	N20 G4 T8
N30 G1 X-2	N30 G1 Y-2
N40 G4 T8**}** Repeat 10 times	N40 G4 T8**}** Repeat 10 times

Test Methodology to quantify X, Y and Z-axis repeatability:

1. Calibrate the LDS to the build platform (follow the steps shown in section 4.1.1 to calibrate the LDS to a surface)
2. Zero the LDS to the surface of the build platform
3. Zero the printer's axis to be tested
4. Record the value displayed by the LDS (value should be close to 0mm)
5. Execute the G-Code
6. The machine will translate the axis negative according to the set value described in the G-code (i.e. G1 X-2)
7. A dwell of eight seconds allows the stabilization of the LDS value
8. Record the stabilized value displayed by the LDS within the dwell time
9. Repeat steps 4,6,7, and 8 for 10 times

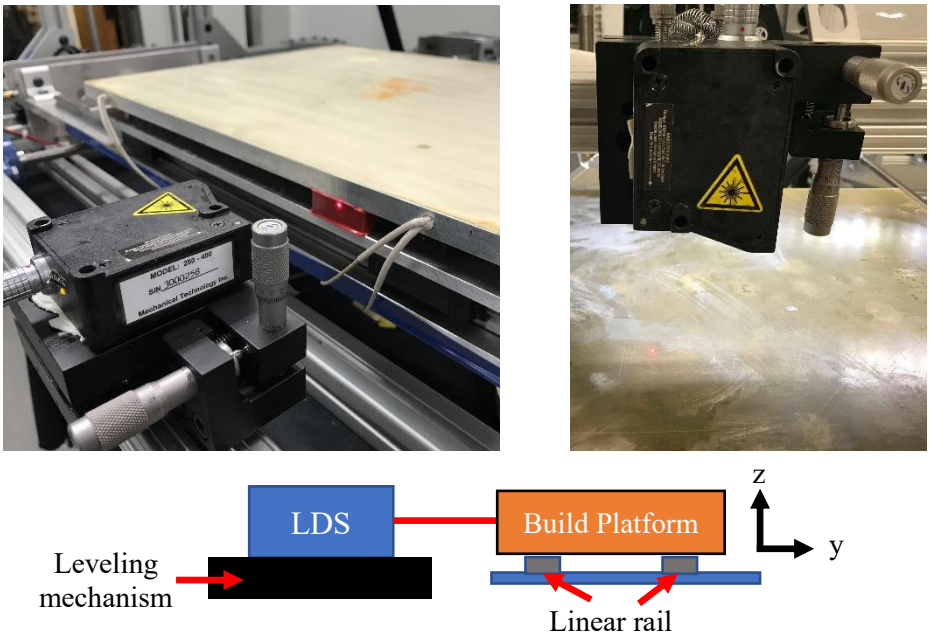

Figure 15 Repeatability of XYZ axes tests

The laser displacement sensor has a 10 mm range, therefore, steps 1-9 were also performed for 5mm displacements by changing the G-code line for motion (i.e. N30 G1 Z-2 to N30 G1 Z-5). Translating a greater distance was believed to increase the percent error due to the lead screw accuracy (for Z-axis lead screws, the manufacture lists ±0.75mm/m of accuracy).

4.2. Heat transfer on build platform

When polymers such as ABS are exposed to thermal differences they develop thermal stresses, and because of this, the polymer warps and printing can fail due to adhesion problems or collision of the plastic part with the nozzle due to delamination. To reduce the thermal stresses, it was necessary to maintain the part just below the glass transition temperature of the polymer. Therefore, a controlled heated bed was implemented to reduce thermal stresses that may affect the part quality and adhesion.

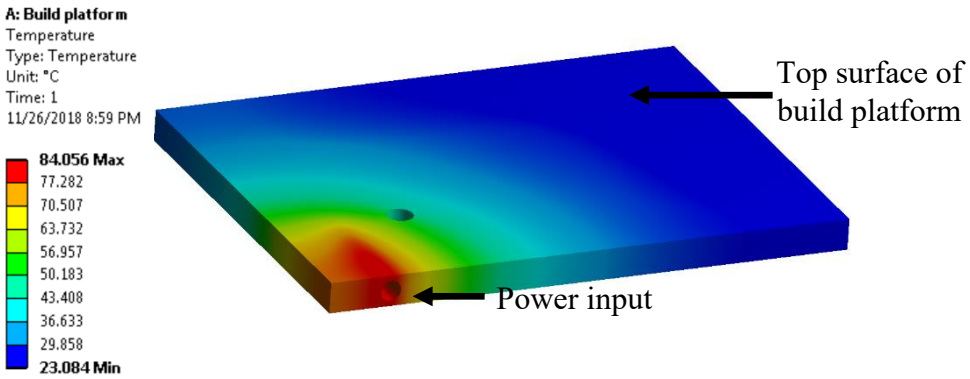

Figure 16 Computational heat transfer model

A steady state heat transfer analysis was performed utilizing ANSYS (ANSYS Inc., Canonsburg, PA), a mechanical simulation software using natural convection to obtain the heat transfer coefficient. Appendix A shows a MATLAB code used to obtain the heat transfer

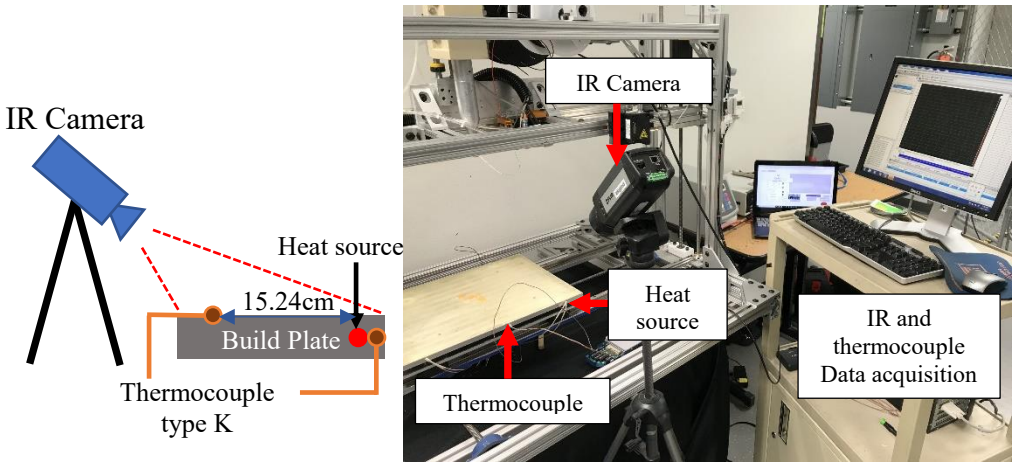

Figure 17 Schematic or build platform temperature

coefficient of 7.61 W/m^2*K. The heat transfer coefficient value was set as an input for the heat transfer simulation. To reduce the computational time, only a quarter of the build plate was analyzed using a 200W power input at the interface shown in Figure16. The maximum recorded temperature of 84ºC obtained with the ANSYS analysis.

To validate the computational method, the following experimental setup was developed (Figure 17). An infrared (IR) camera was used to record the temperature of the build plate. The build platform was set to 120ºC for about 30minutes. At the same time, a thermocouple type K was placed 15.24cm (6in) away from the heat source and on the surface of the bed to compare and experimentally fit the emissivity value given to the IR camera. Another thermocouple was placed next to the heat source where the IR camera was focused. This comparison was used to get an idea of the temperature distribution along the aluminum 6061 plate. If a large temperature different was seen on the build platform, the placement of additional cartridge heaters would help maintain a more uniform temperature distribution along the build plate.

4.3. Accuracy of extruded lines

The extruder gear ratio was determined by jogging the extruder stepper motor for one millimeter. The liquefier was set to 240ºC with a nozzle size of 0.4mm and loaded with ABS plastic filament. The actual extruded amount of material was measured with a digital caliper and a gear ratio of 1:30 was obtained by trial and error. A small G-code was executed to extrude five different line sizes: 10, 20, 50, 100 and 150mm and created the extruded lines in Figure 18. The speed and acceleration were kept constant at $20\,{}^{mm}/_{s}$ and $800{}^{mm}/_{s^2}$, respectively. The filament retraction between extruded lines distance and speed were set to 6mm at $800{}^{mm}/_{s^2}$, respectively.

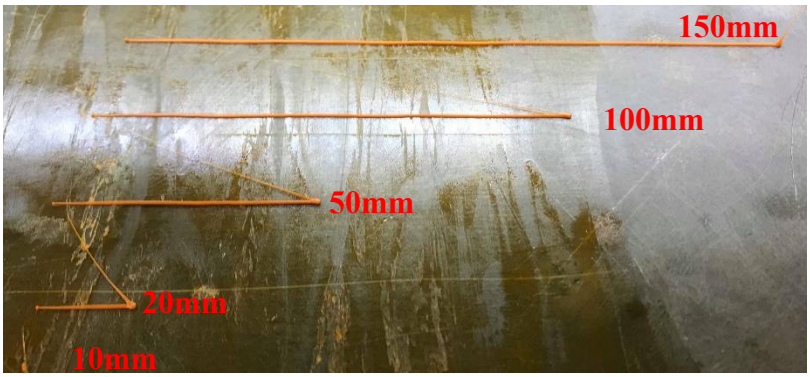

Figure 18 Extruded lines with varying distances

4.4. Ranking Model

A ranking model inspired by the NIST AM testing artifact reported by Moylan *et al.* (2012) was used to compare the dimensional accuracy of the modular desktop 3D printer to that of a production grade material extrusion printer. The modified ranking model (Perez, 2013) had dimensions of 77mm x 77mm x 16.35mm and a volume of 40531.48mm^3. The modular desktop 3D printer was configured with a 0.4mm nozzle and a constant acceleration of 800mm^3. The Cura

Table 4 Parameters for printing PLA

layer height	0.25 mm
line width	0.5 mm
infill	100%
infill layer thickness	0.25 mm
print speed	60 mm/min
infill speed	60 mm/min
extrusion temperature	220ºC
platform temperature	80ºC

slicer (Ultimaker, Cambridge, MA) was used to slice the PLA ranking model used to characterize the modular desktop 3D printer with the parameters shown in Table 4:

Once the G-code file was generated using the listed parameters mentioned above, the G-code was modified by a post-processor that changed the structure of the G-code to be accepted by the PAC controller used on the modular desktop 3D printer. The changes involved the implementation of "N <line number>" at the beginning of each line in the G-code. Additionally, extrusion values expressed as "E" by Cura where changed to "P". Finally, the header "N<line number> G1 F<velocity> E<acceleration> E<deceleration>" was implemented. The same ranking model was printed using a Fortus 400mc (Stratasys, Eden Prairie, MN) FDM printer using a nozzle size of 0.254mm (0.010in). The material used was PC at its highest density option. Features

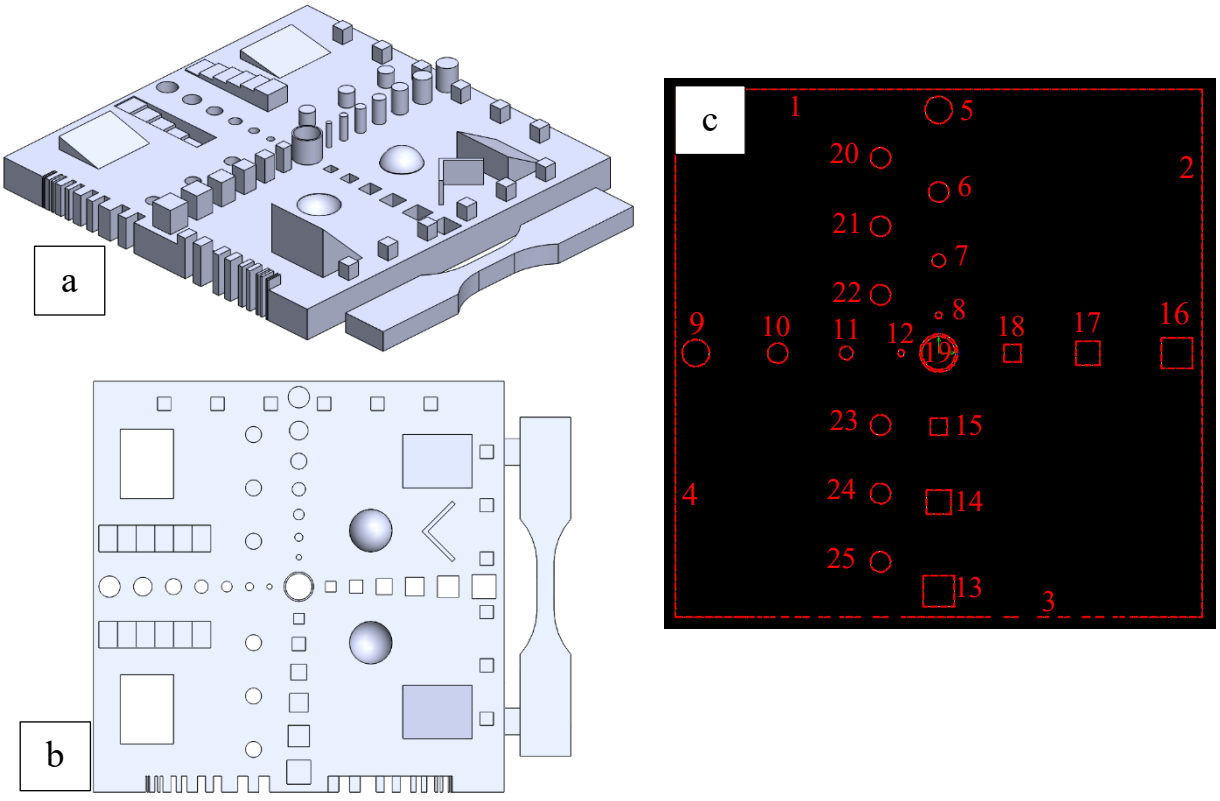

Figure 19 Modified version of CAD Ranking model (a) isometric view (b) top view (c) points of interests measured by the optical measuring tool.

contained by the ranking models were measured with the help of a SmartScope Flash 250 (OGP, Rochester, NY) optical measuring tool. Figure 19 shows the ranking model used to perform the comparison.

The following list describes the features compared for both printed ranking models along with the CAD ranking model:

- length of each side of the ranking model (figure 19(c): 1-4)
- varying circular extrusions (figure 19(c): 5-8)
- varying circular cut extrusions (figure 19(c): 9-12)
- varying square extrusions (figure 19(c): 13-15)
- varying square cut extrusions (figure 19(c): 16-18)
- circular cut extrusion (figure 19(c): 19)
- repeatability of circular extrusions (figure 19(c): 20-22)
- repeatability of circular cut extrusions (figure 19(c) 23-25)

4.5. Surface Roughness

Figure 20 shows a surface roughness tester, SURFTEST SJ-210 (Mitutoyo, Aurora, IL), was used in compliance with the ISO1997 standard to compare a fully dense PC FDM surface to

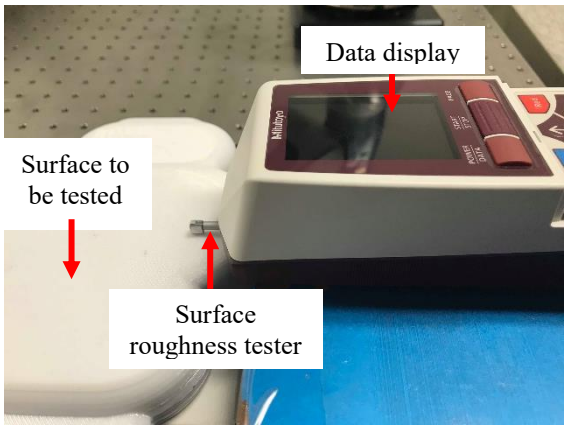

Figure 20 Surface roughness tester

a fully dense ABS printed part using the modular desktop 3D printer. A stylus tip detector with a radius of 5μm, a measuring force of 4mN, and a tip angle of 90º was used. The stylus detector performed five measurements each at 8.12μm at 5mm/s. In addition, three different tests were performed for each substrate to obtain an average and standard deviation.

4.6. Characterization of Wire Embedding

Parameters for wire embedding were developed for the modular desktop 3D printer using the following strategy. Figure 21 (1) shows the wire embedding tool as it approached the substrate loaded with wire to initialize embedding. The wire embedding tool was engaged at the same moment that the tool began its path along the surface of the polymer, Figure 21 (2). In most cases, the mechanical grip from the polymer to the wire happened instantaneously without any external reaction forces as the tool traversed along the polymer's surface, Figure 21 (3). When the tool finished its trajectory, the tool was turned OFF to stop the energy input from the ultrasonic horn to both the wire and substrate as shown in Figure 21 (4). To finish the embedding process, the tool was translated away from the substrate and the cutting mechanism was engaged to start the wire embedding process again, Figure 21 (5).

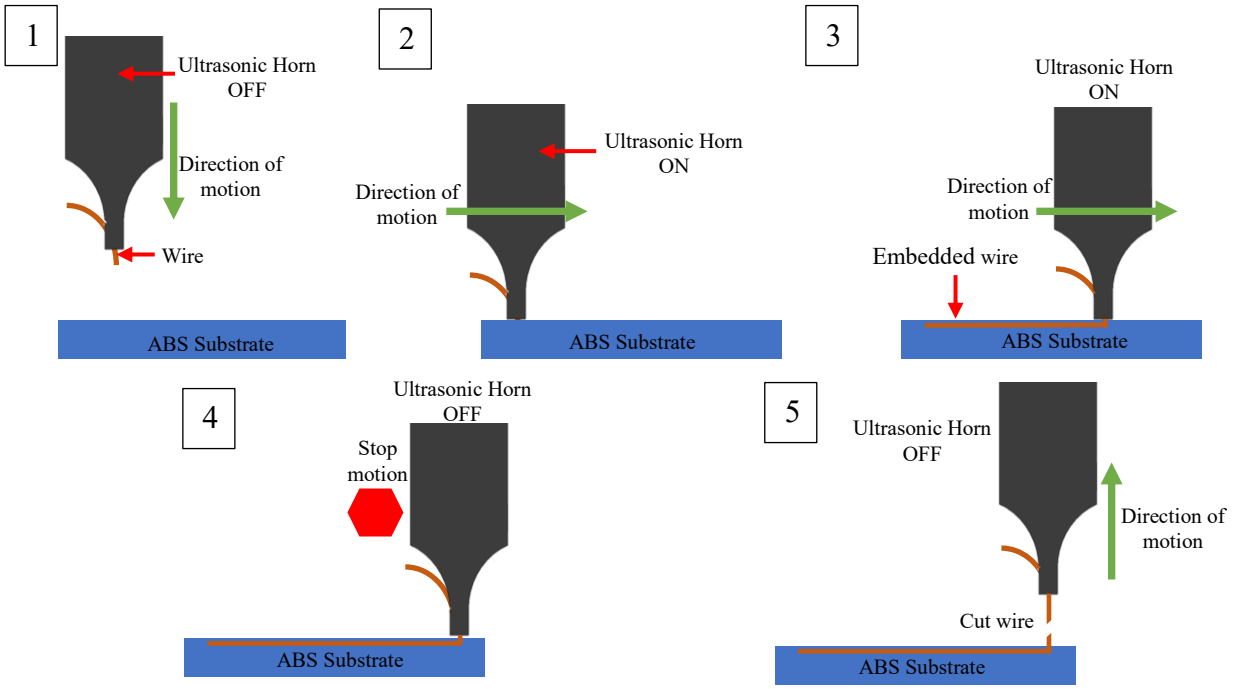

Figure 21 Progression of wire embedding process

4.7. Characterization of parallel traces

To understand the variance of the distance between two parallel wires, a 5.0cm x 7.62cm x 1.25mm fully dense ABS plastic substrate was printed and three parallel wires were embedded. The first parallel pair was spaced 10mm apart from center-to-center, the second pair was spaced 1mm apart, and the third pair was spaced 0.5mm apart. Embedding the 26AWG copper wire was possible with the parameters gather from the previous experiment. The part was inspected on a SmartScope Flash 250 optical measuring tool and an average was obtained for the 10mm, 1mm, and 0.5mm using three different measurements for each pair.

4.8. Characterizing parallel traces with varying angles

Figure 22 shows the fabrication of four ABS coupons measuring 50.8 x 101.6 x 1.25 mm (2in x 4in x 1.25mm) with embedded wires to understand the capabilities of wire embedding when sharp turns are required. Each coupon had three parallel traces to quantify the consistency in spacing between the trace pairs. Four coupons with distinct angles (135º, 90º, 60º, 35º) were fabricated. The variation of angles helped to determine the minimum angle to be fabricated using the ultrasonic horn before failure occurred by not embedding at all. An embedding speed of 8mm/s and an amplitude of 60% was used to fabricate the test coupons.

Figure 22(e) shows the expected results and measurement approach. Instead of a sharp wire turn, a more circular feature was expected as noted in section 2. Since section 2 was expected to be circular, three measurements were obtained to better describe the distance between the pairs. Section 1 and section 3 measurements were simply obtained by measuring the center-to-center distance between the two pairs using the SmartScope Flash 250 optical measuring tool.

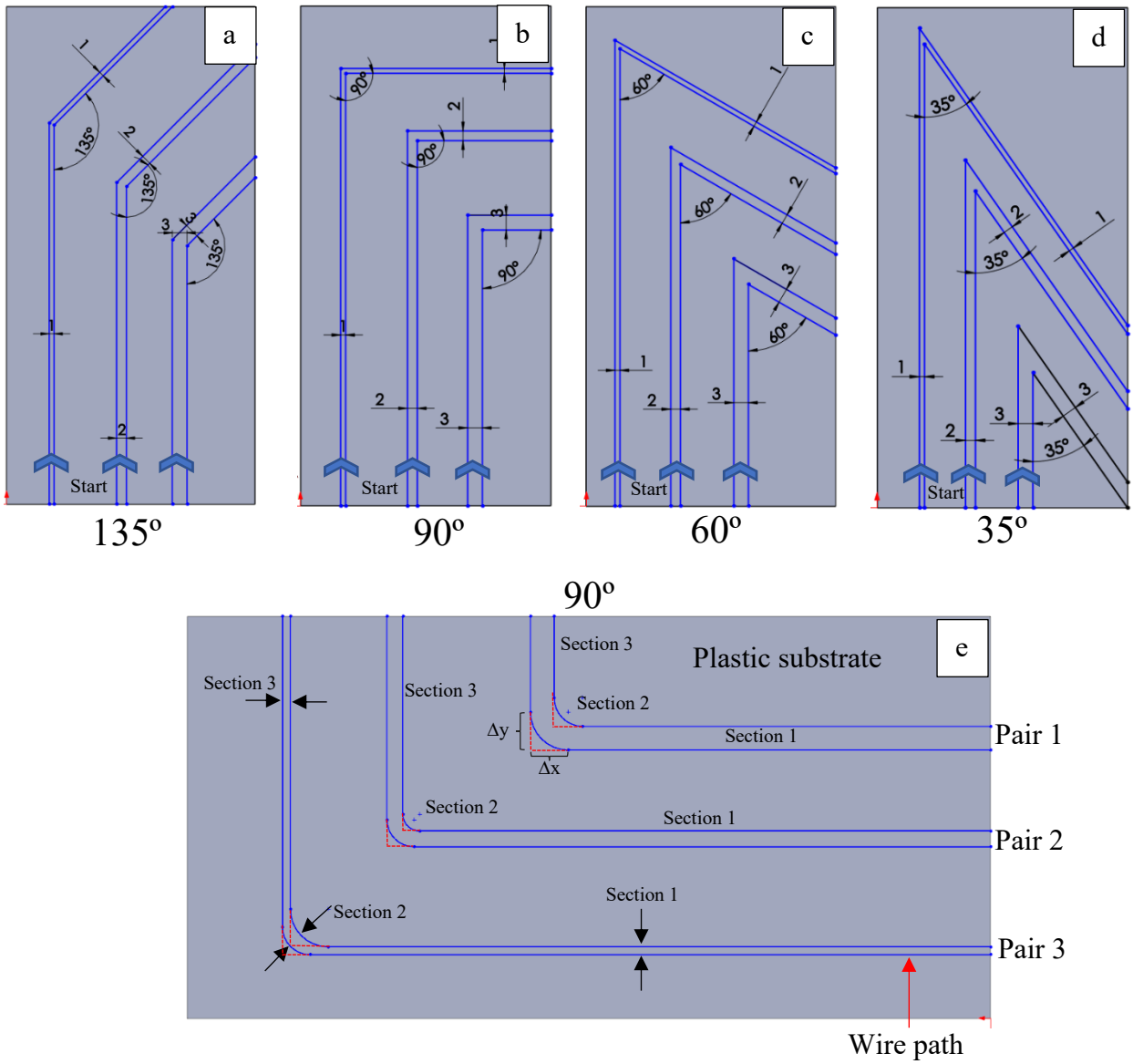

Figure 22 Test coupons of parallel 26 AWG wire traces with different angles (a) 135º (b) 90º (c) 60º (d) 35º. Each test coupon contained three pairs spaced at 1mm, 2mm and 3mm apart from center-to-center. (e) three sections where measurements were taken.

CHAPTER 5

RESULTS

5.1. Test 2. XYZ-axis repeatability

Table 5 shows the results for the calibration of the displacement sensor. A standard deviation was obtained for both the 2.54mm and 5.08mm rectangular gauges. As shown in Table 5, the standard deviation for the 2.54mm and 5.08mm rectangular gauges were ±4.41µm and ±4.45µm, respectively. Comparing the standard deviation from the performed tests with the LDS resolution (±2.54µm) shows that there is a 2µm difference, which in most material extrusion printers, the minimum printing features is 254 µm (Espalin *et al.*, 2013). Therefore, it was concluded that the 2µm difference may be considered negligible since the printer itself may not print with such accuracy. An average percent error was also calculated for the LDS for both the 2.54mm and 5.08mm gauge blocks being 1.98% and 1.35% error, respectively. These results conclude that the laser's accuracy may be affected by the position of the LDS whenever it was calibrated using the leveling mechanism.

Table 5 Percent error and standard deviation for the Laser Displacement System

Feeler Gauge	Standard Deviation mm	Average % Error
2.54 mm	0.0441	1.98
5.08mm	0.0445	1.35

The following results were obtained by performing the repeatability tests for the X-, Y- and Z-axis. Table 6 shows the standard deviation and percent error of nine repetitions (see Appendix B) for the 2mm and 5mm displacements of each axis. The standard deviation of the Y-axis was ±0.6µm and ±0.5µm with an average error of 0.12% and 0.11% for the 2mm and 5mm

travel displacements, respectively. The X-axis also showed a similar deviation of ±0.60 μm and ±1.63 μm and a percent error of 0.11% and 0.18% for the 2mm and 5mm travel displacements, respectively. Finally, the Z-axis showed a standard deviation of ±0.83 μm and ±0.78 μm and a percent error of 0.32% and 0.16% for the 2mm and 5mm travel displacements, respectively. The laser displacement shows a similar trend to the percent error shown in Table 6 for the 2mm and 5mm gauge block. The laser accuracy of ±0.1% was obtained from the manufacturer, therefore, the percent error of the 2mm and 5mm travel displacements is range. Keeping in mind that the laser has a resolution of ±2.54μm, the average percent error may be present due to the laser's calibration, however, the accuracy of the lead screws ~±0.75mm/m (±0.009in/ft) may also be a contributing factor.

Table 6 Repeatability results for XYZ axes

Y-axis travel distance	Standard Deviation μm	Average % Error
2mm	0.60	0.12
5mm	0.50	0.11
X-axis travel distance	**Standard Deviation μm**	**Average % Error**
2mm	0.60	0.11
5mm	1.63	0.18
Z-axis travel distance	**Standard Deviation μm**	**Average % Error**
2mm	0.83	0.32
5mm	0.78	0.16

It is easy to see that the largest percent error was obtained by the Z-axis, however, 0.32% may be important since it will noticeably impact z height. 0.032 is 813 microns, which is equivalent to approximately three 254-micron layers. If the position is low, the extruder will collide with the deposited material. On the other hand, if the extruder is high, the deposited material will not adequately bond with the underlying material.

5.2. Heat transfer on build platform

Figure 23 shows the schematic of the temperature experiment. A maximum temperature of ~120ºC was seen on both the thermocouple sensor and IR camera. The temperature at the heat source reached ~120ºC in 8 minutes for both the IR camera and the thermocouple located next to the heat source. The thermocouple at the surface reached a temperature of ~100ºC in about 14 minutes. After the 14 minutes the temperature reaches steady state at about ~100ºC.

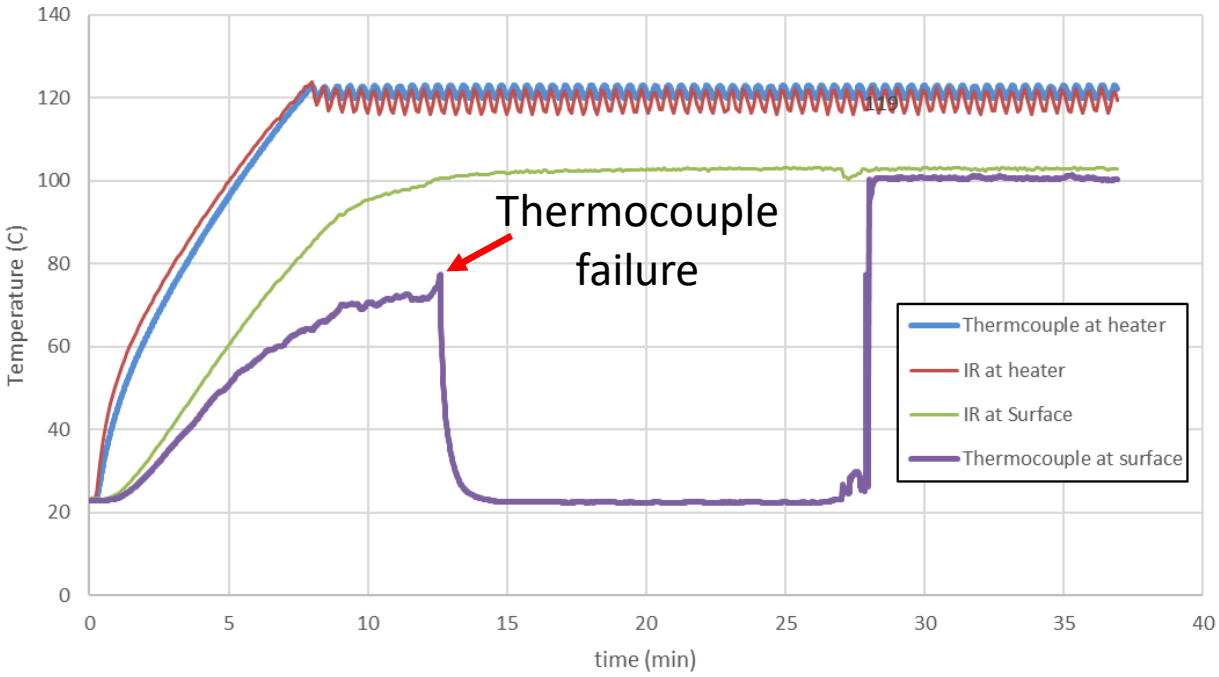

Figure 23 Temperature experiments

5.3. Accuracy of extruded lines

Ten different trials were printed and measured using a digital caliper to obtain an average and standard deviation, as seen on Figure 24, of the set extruded lengths to compare to the actual extruded beads. Looking at the outermost cases, the bead that is set to measure 10mm has a measurement of 10.34±0.64mm and the bead that is set to measure 150mm has an actual measurement of 151.93±0.58mm. A trend was not detected with the increase of distance and the error accumulated. To obtain more precise results when compared to the actual distances, the amount of filament to be retracted and the retraction rate is believed to be the most influential parameters.

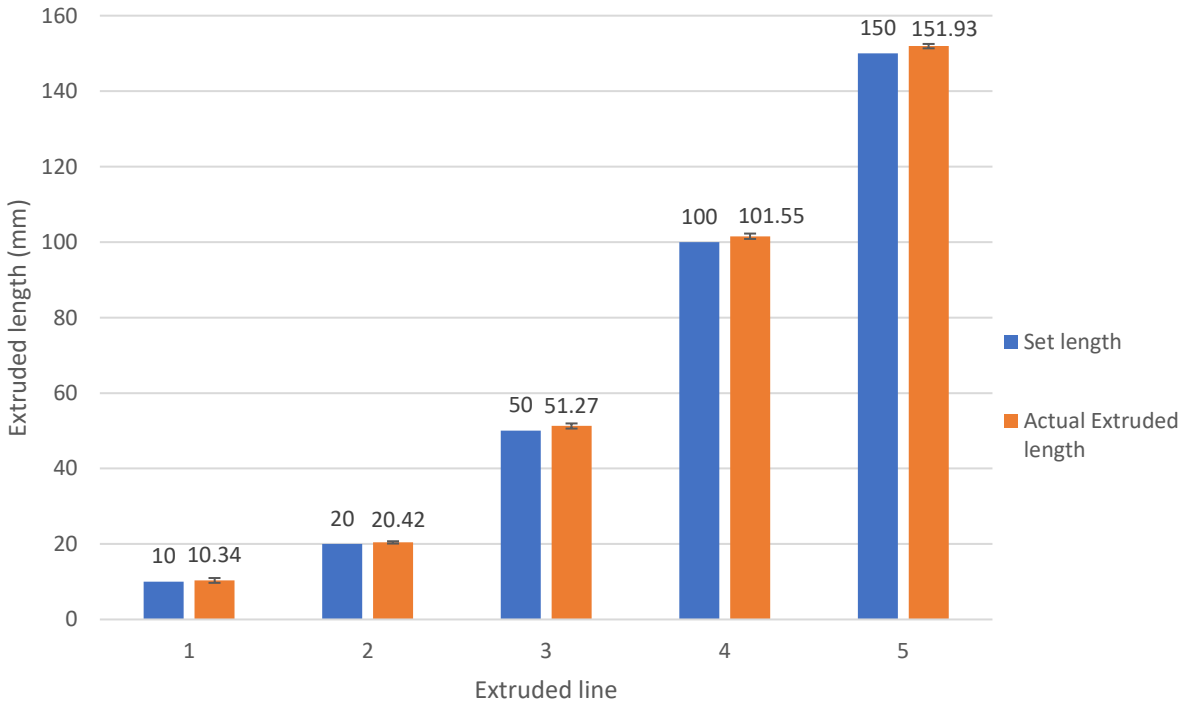

Figure 24 Comparison of set extruded lengths and actual extruded lengths

5.4. Ranking Model

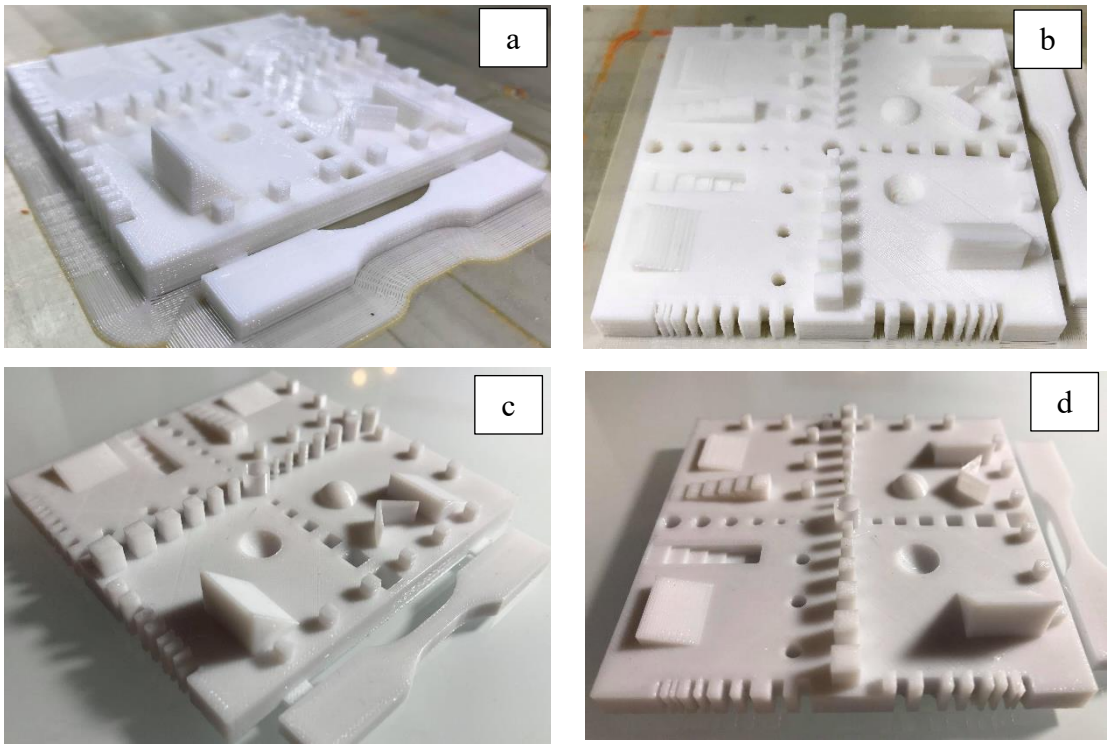

Figure 25 3D printed ranking model used for printer comparison (a) isotropic view of printed part using the modular desktop 3D printer (b) front view of printed part using the modular desktop 3D printer (c) ranking model printed with Fortus 400mc (d) front view of printed part using Fortus 400mc

Figure 25 shows the fabricated ranking models used for comparison. Figure 25(a and b) shows the PLA fabricated part using the modular desktop 3D printer. Figure 25(c and d) shows the PC fabricated part using the Fortus 400mc FDM printer. Figure 26 shows a comparison of the dimensions of the CAD (blue), the FDM-printed part (gray), and the PLA part printed by the modular desktop 3D printer (orange) for the square extrusion features. It is easy to see that the features have very similar results when compared to the actual CAD model. For example, “feature 13” shows a 0.56% error for the FDM printed part and an error of 2.82% for the modular desktop 3D printer. Appendix C shows the features measured for feature 1-25. For example, feature 1-4 for the modular desktop 3D printer always showed oversized features, the largest being “feature 1” with a percent error of 1.46% (1.12mm difference when compared to the CAD model). Also,

in Appendix C, results for the circular extrusion features, for example, “feature # 7” shows a 5% error on the FDM printed part and a 16% error for the modular desktop 3D printer

Features 20-25 (Figure 27) shows the repeatability of the printer by printing the same feature three times. The features produced were a circular extrusion (features 20-22) and a circular cut extrusion (features 23-25) ideally measuring 3mm in diameter. Features 20-22 for the FDM produced PC ranking model showed an average of 2.89 ± 0.06mm and the PLA produced ranking model showed an average of 2.93 ± 0.08mm for the same features. When generating the circular extrusion features, the modular desktop 3D printer showed a value closer to the CAD when compared to the FDM printed features. Similarly, measurements were taken for the cut extrusion features 23-25 for both the FDM printed part and the modular desktop 3D printer and resulted with an average of 2.96 ± 0.04mm and 2.65 ± 0.08mm, respectively. Features 23-25 where much more defined for the FDM when compared to the modular desktop 3D printer which undersized the features. It is possible to see that a larger percent error occurs on the modular desktop 3D printer, however, this was expected as the FDM printer has been the industry standard for rapid prototyping.

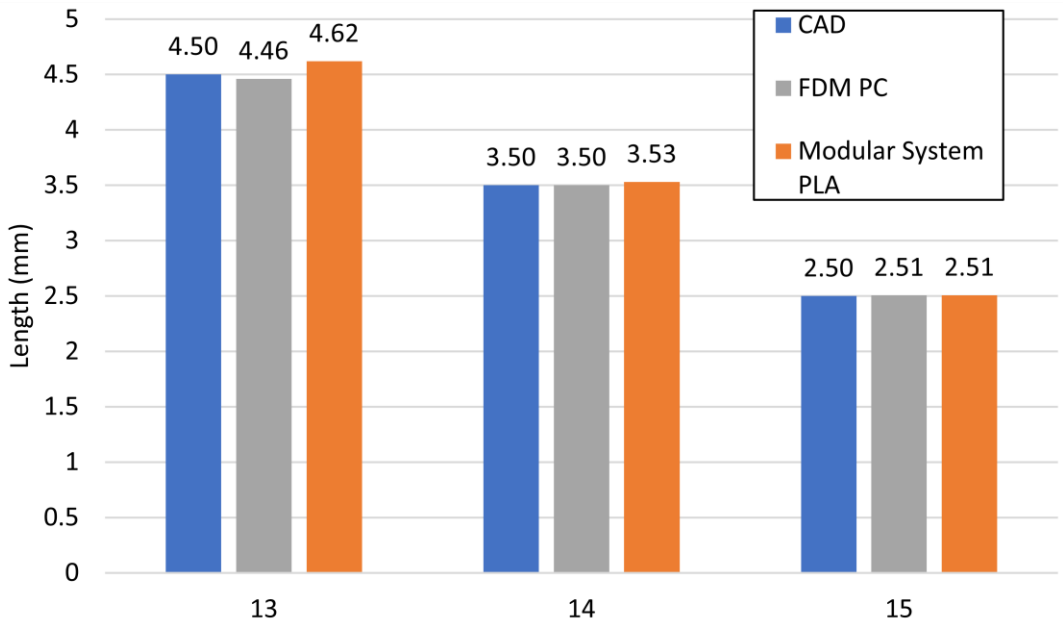

Figure 26 Graph showing the average in dimensions of square extrusions with varying lengths. Comparison of CAD model, FDM industry grade 3D printer, and the developed modular 3D system.

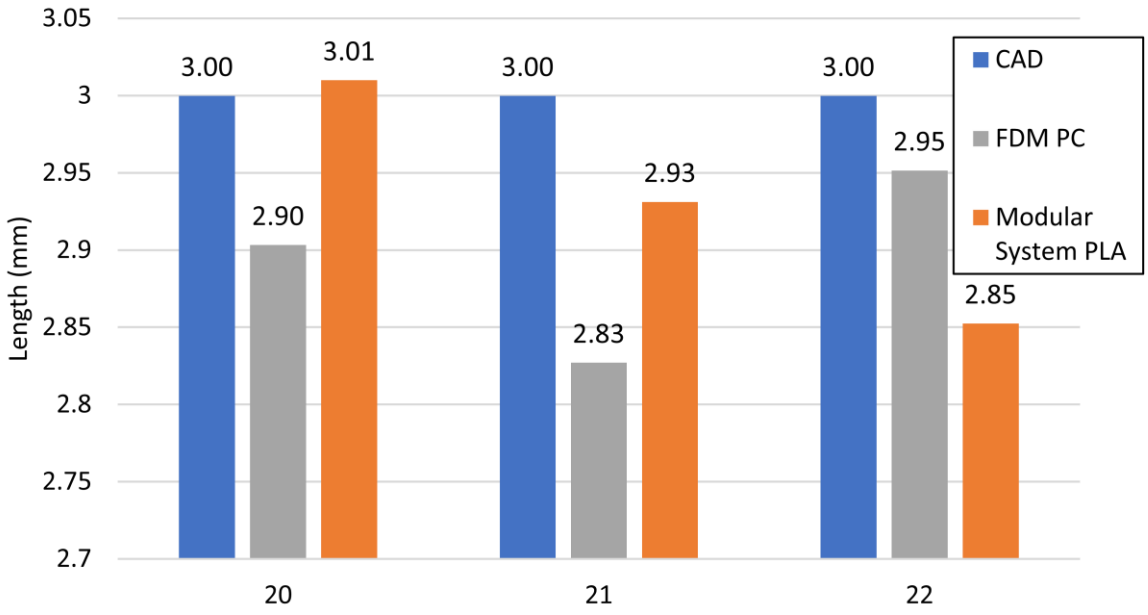

Figure 27 Graph showing the average in dimensions of extruded cylinders having the same diameter. Comparison of CAD model, FDM industry grade 3D printer, and the developed modular 3D system

5.5. Surface Roughness

A roughness test comparison between a dense PC FDM (using a 0.4mm extrusion nozzle) printed part and a 100% dense ABS part fabricated with the modular desktop 3D printer (using a 0.4 mm extrusion nozzle). The FDM production grade 3D printer resulted with a surface roughness of 16.59 ± 0.05µm. The modular desktop 3D printer obtained a surface roughness of 11 ± 0.04µm resulting in a smoother surface. By simply touching the ABS produced part compared to the PC FDM printed part it was obvious to feel a smoother surface. This may be due to the difference in part densities due to the extruder gear ratio of the modular desktop 3D printer. That is, the gear ratio was obtained experimentally as shown in section 4.3, therefore, the extrusion rate is different for both printers which may impact surface roughness due to the lack of extruded material by the modular desktop 3D printer when compared to the FDM Fortus 400mc.

5.6. Characterization of Wire Embedding

Parameters were obtained for embedding 26AWG (Ø = 405 µm) copper wire by printing 25 fully dense ABS coupons measuring 25.4 mm x 12.7 mm x 12.7 mm (1in x 0.5inx 0.05in). Using an aluminum ultrasonic homogenizer control, the amplitude was kept constant at 60% while the traversing speed was varied from 7 to 11 mm/s at 1 mm/s increments. Typically, ultrasonic horns are made from titanium, however, the ultrasonic horn was custom made from aluminum to easier modify/machine features (i.e. central channel for wire feeding). The build platform target temperature was kept constant at 100ºC during the embedding process. Trial and error experiments were performed until embedding was successful using the conditions stated above. The wire was held with needle-nose pliers to help with the adhesion between the polymer and the copper wire. Figure 28 shows the results of embedding for the first time using the modular desktop 3D printer.

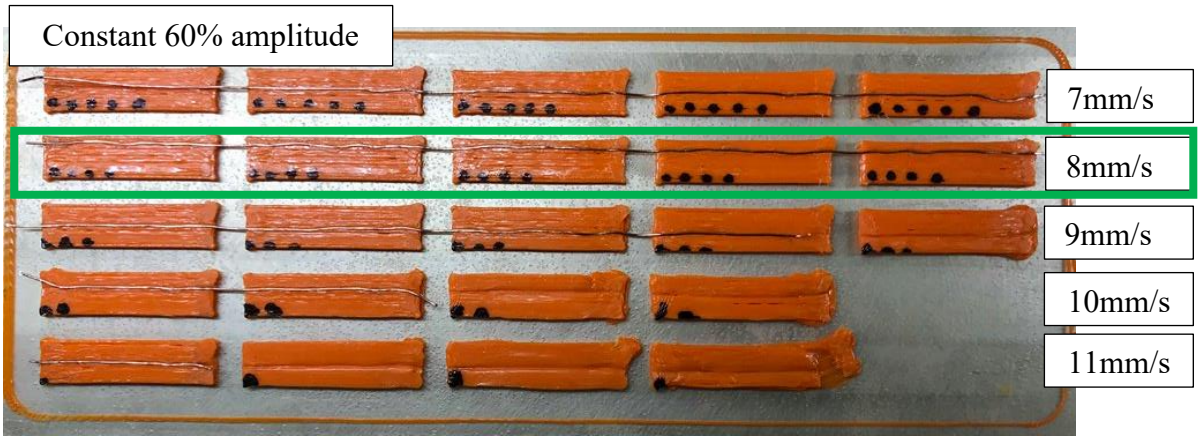

Figure 28 Varying embedding speeds with constant ultrasonic amplitude. 8mm/s was the speed that embedding happened 100% of the times.

Five trials were performed using an embedding speed of 8mm/s with the constant ultrasonic amplitude of 60%. A 100% success rate was achieved when embedding at 8mm/s at 60% amplitude, therefore, this document will use these two parameters when embedding 26AWG solid copper wire onto an ABS plastic substrate. The following experiments were developed to further characterize the quality of wire embedding.

5.7. Characterization of parallel traces

An average value of 10.31mm, 1.16mm, and 0.70mm were obtained for the 10mm, 1mm, and 0.5mm center-to-center distances, respectively. It was concluded that the variance in the spacing was caused due to the large tolerance that the nozzle of the ultrasonic horn has over the 26AWG wire. The exit diameter of the ultrasonic horn is 1.5mm when compared to the wire diameter (0.405mm), therefore, the wire has enough space to move around when exiting the horn. Figure 29 shows the fabricated ABS substrate with parallel copper wire traces.

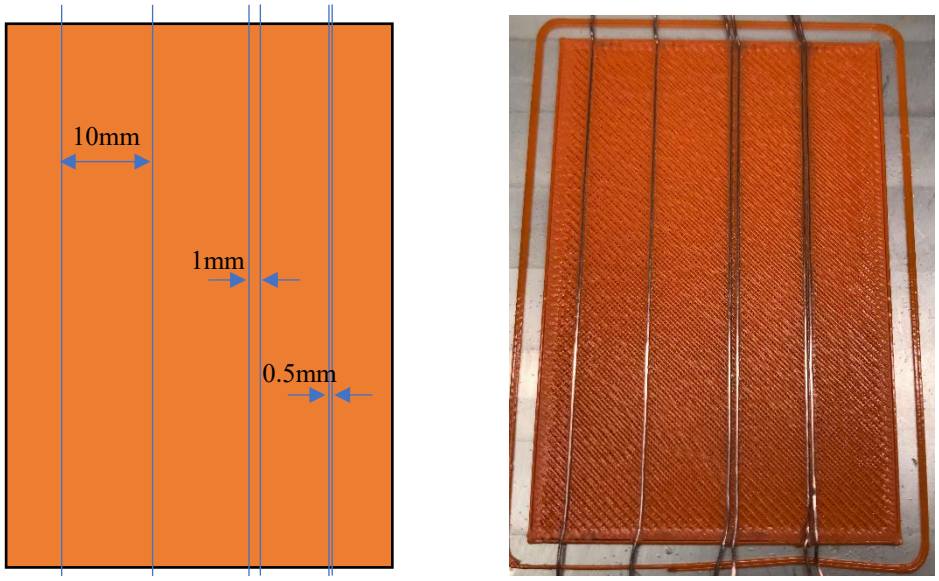

Figure 29 Schematic (left) of printed part (right) containing parallel 26AWG wire traces

5.8. Characterizing parallel traces with varying angles

Figure 30 shows the fabricated test coupons containing parallel wire traces with different angles. As expected, no sharp turns are observed on any of the printed samples, instead, a slight arc is detected due to the large tolerance that the wire embedding exit diameter (1.5mm) has over the diameter of the copper wire (0.405mm). Figure 30(a) shows desirable embedding when compared to Figure 30(c) or Figure 30(d). Since the angle is smaller in Figure 30(d), the ultrasonic horn has a larger energy input due to the sharp turn when compared to Figure 30(a) where embedding is continuous.

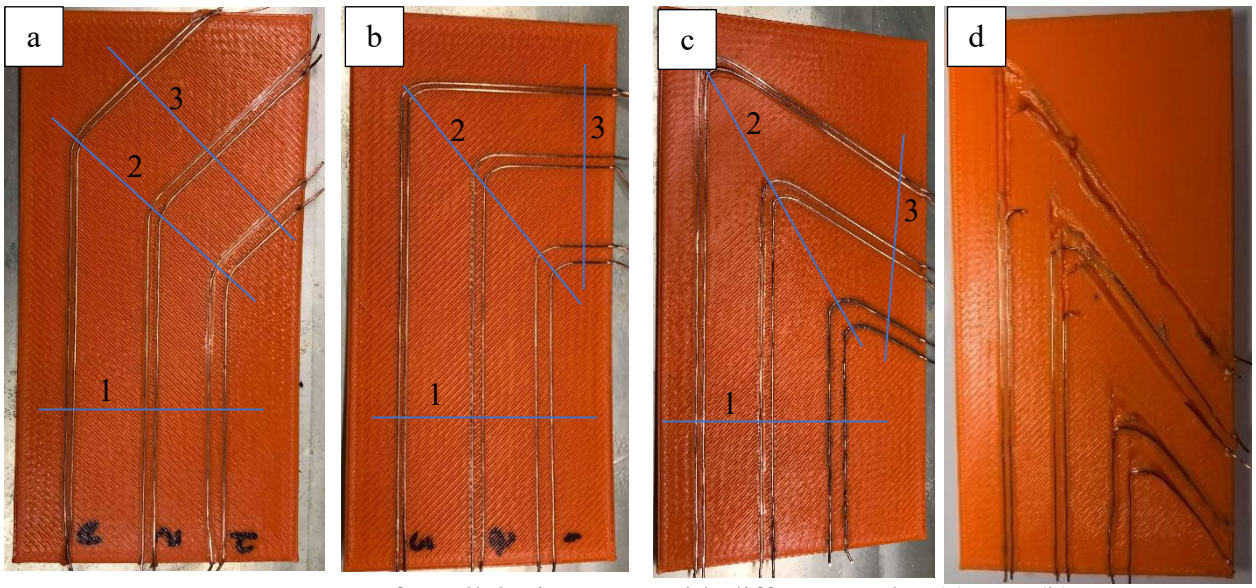

Figure 30 Test coupons of parallel wire traces with different angles (a)135º (b)90º (c)60º (d)35º

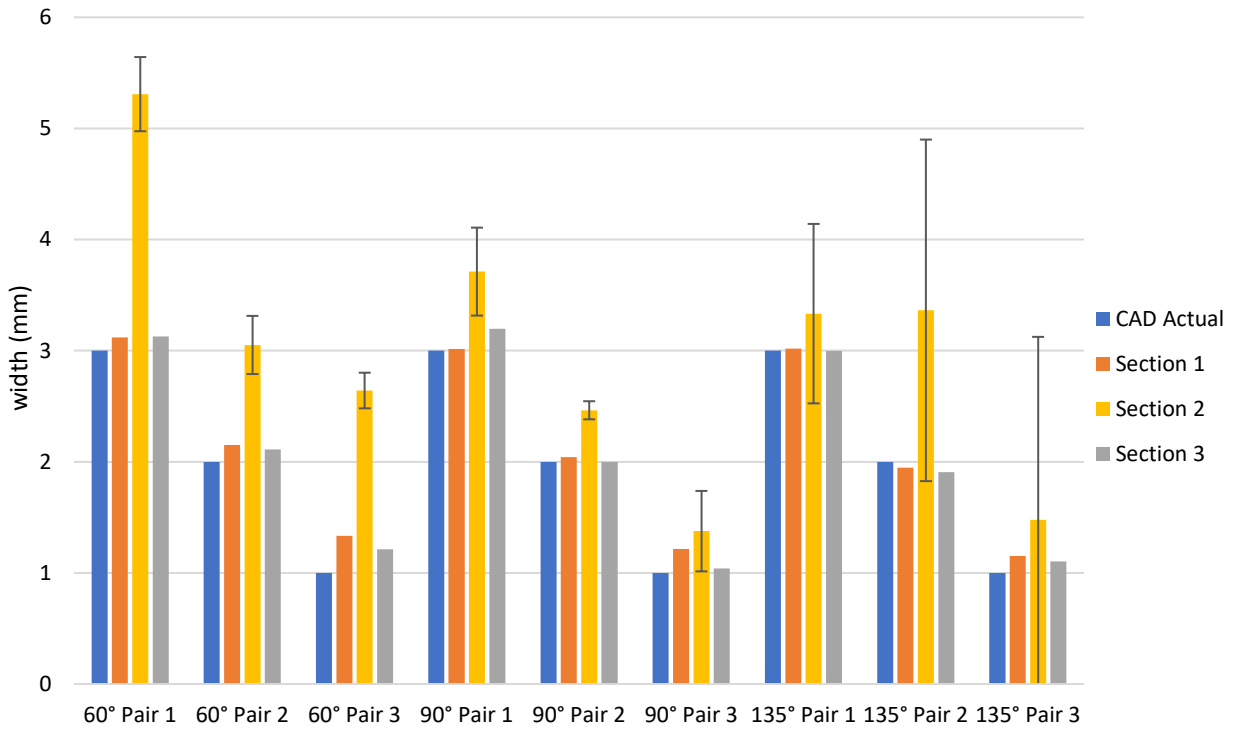

Figure 31 Measurement results for parallel wire widths

Figure 31 shows the measurements taken by using the SmartScope Flash 250 optical measuring tool. The graph is divided by the angles of each test coupon and their corresponding pairs compared to the actual CAD measurements. Section 1 and 3 show very similar results when compared to the CAD, for example, pair 1 with an angle of 60º shows a value of 3.11mm for section 1, and 3.12mm for section 3. However, section 2 shows a value greater than 5mm. This large variance is believed to happen because of three reasons:

- the large tolerance inside the wire embedding nozzle allows the wire to freely move side to side
- the pull that the wire is exposed to when embedding

Section 2 also shows larger variances in width when compared to the actual CAD dimensions for the test coupons (Figure 31). For each pair, two circles were fitted within the arc

and a center to center distance was measured to represent the width of section 2. Three measurements were obtained for each pair in section 2 to obtain the error bars. Section 2 for the 135º test coupon showed the largest error bars due to the variance in the circle diameter used for fitting the arcs.

A test to understand when the arc starts to form Δx and Δy displacements (refer to Figure 22(e)) was also performed. The average of when the arc starts to form Δx and Δy (refer to Figure 22(e)) was obtained for each angle. Table 7 shows the results for Δx and Δy:

Angle	Δx Avg (mm)	STDEV (mm)	Δy Avg (mm)	STDEV (mm)
60	5.942	0.904	6.088	0.337
90	3.512	0.516	4.857	1.380
135	3.734	0.902	3.183	0.699

Table 7 Δx and Δy angle variance

The data provided above allows for design constraints. If the user wishes to place a component or a feature next to a wire trace with a sharp angle the trace, the wire may interfere with the component as seen in Figure 32. It is safe to conclude that the distance between pairs can increase up to 75% from the set width at sharp turns. Additionally, design constrains for component placement next to wires with changing direction were defined to avoid component interference with wire traces.

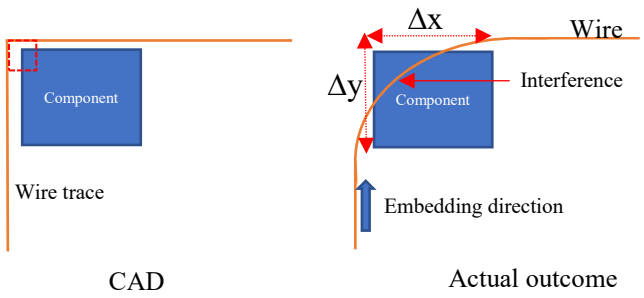

Figure 32 Component and wire trace interface

Part Demo

To test the multi-functionality of the modular desktop 3D printer, a test ABS part of dimensions 10mm x75mm x2mm was constructed using a 0.4mm orifice nozzle on a MK8 Direct Drive extruder. The printing material was set to 240ºC and the bed temperature was set to 120 ºC. Speeds and accelerations were set constant at 60mm/s and $80mm/s^2$, respectively. A rotary spindle tool mainly used for metalworking was implemented in the modular desktop 3D printer by printing a plastic PLA mount to attach on the Z-axis aluminum extrusion tool holder next to the material extrusion and wire embedding tool. Machining parameters were not optimized as the

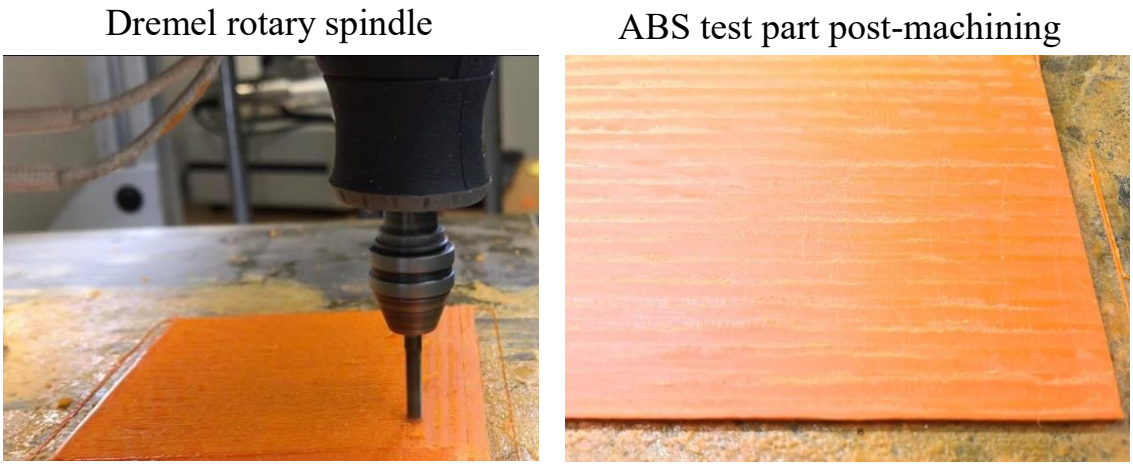

Figure 33 Machining capabilities on the modular desktop 3D printer

intent of this study was to prove the fabrication of generating multi-functional parts and implementing modularity to the printer. This was accomplished by implementing wire embedding and a rotary spindle on the material extrusion printer. Machining was performed using a feed speed of 8mm/sec with pressurized air for cooling. Figure 33 shows the machined fabricated part.

CHAPTER 6

CONCLUSION AND FUTURE WORK

6. CONCLUSION

A modular desktop 3D printer was designed and constructed with most "off-the-shelf" components. The printer was assembled within an estimated time of two hours with common tools. The printer was designed and evaluated using a force analysis of the Z-axis lead screws to lift a payload of 68kg (150lbs), therefore, NEMA 23 stepper motors were chosen to satisfy the requirement. The printer allowed a maximum payload of 86kg (190lbs) when the load was at the center of the Z stage. A finite element analysis using SolidWorks static study that resulted in a maximum von Mises stress of 233.9MPa at the alloy steel rail. An MK8 direct drive extruder that allowed materials with extrusion temperatures ≤ 300ºC. For wire embedding, a Cole-Parmer Instruments (Illinois, USA) ultrasonic homogenizer was used with a power of 500Watts and a frequency of 20KHz to embed solid wire of 32-24AWG onto a plastic substrate.

A Parker Automation Controller (PAC) was chosen due to its modularity and low price when compared to Yaskawa and Delta Tau programmable logic controllers and motor drivers. A human machine interface (HMI) was developed using the Parker Automation Manager (PAM) to control the modular desktop 3D printer. G-code was uploaded to the PLC via PAM software and the G-code was executed by the user in the HMI.

Test for repeatability of X-, Y- and Z-axis were performed to characterize the modular desktop 3D printer. The repeatability average percent error of the Y-axis was 0.12% and 0.11% for the 2mm and 5mm travel displacements, respectively. The X-axis showed percent errors of 0.11% and 0.18% and the Z-axis showed a percent error of 0.32% and 0.16% for the 2mm and 5mm travel displacements, respectively.

A temperature test was performed to quantify the heat distribution throughout the build platform. A maximum temperature of ~120ºC was recorded in 8 minutes via an IR camera and

thermocouple sensors. The thermocouple at the surface 15.24cm (6in) away from the heat source reached a temperature of ~100ºC in roughly 14 minutes until reaching steady state.

Parameters and design constraints for wire embedding were developed for the modular desktop 3D printer. A 100% success rate was achieved when embedding straight 26AWG linear traces at 8mm/s and 60% ultrasonic amplitude. In conclusion, a minimum of 60º turn angles can be used when embedding. If wires are placed in parallel, the distance between the pair can vary up to 75% from the set width due to the sharp turns. Additionally, design constrains for component placement next to wires were defined to avoid component interference with wire traces. Parameters for material extrusion and wire embedding were obtained for the modular desktop 3D printer and a printed part with embedded wire was fabricated.

Machining capabilities were easily integrated to the modular desktop 3D printer. A rectangular ABS coupon was faced using a 1/8 end mill. The printer allowed a maximum payload of 86kg (190lbs) when the load was at the center of the Z stage. Therefore, due to the high weight carrying capabilities of this printer, multiple tools can be integrated such as a pellet extruder for large and rapid material deposition. This printer allows for the fabrication of components in remote locations where supplies and manufacturing machines are scarce (i.e. theatre of war, oil rigs). This modular desktop 3D printer may be easily implemented as long as there is a 120VAC power supply.

FUTURE WORK

It was believed that as the turning angles decreased, the wire embedding was prone to failure as it would pull out the wire as seen on the parallel tests with sharp turns of the 35º test coupon (Figure 30 d). It is believed that the failure happens due to excessive amount of accumulated energy input in the same area. That is, when the horn overlaps (or reprocesses) an area, the thermal energy is being accumulated within the polymer causing the polymer to flow and inhibit wire retention.

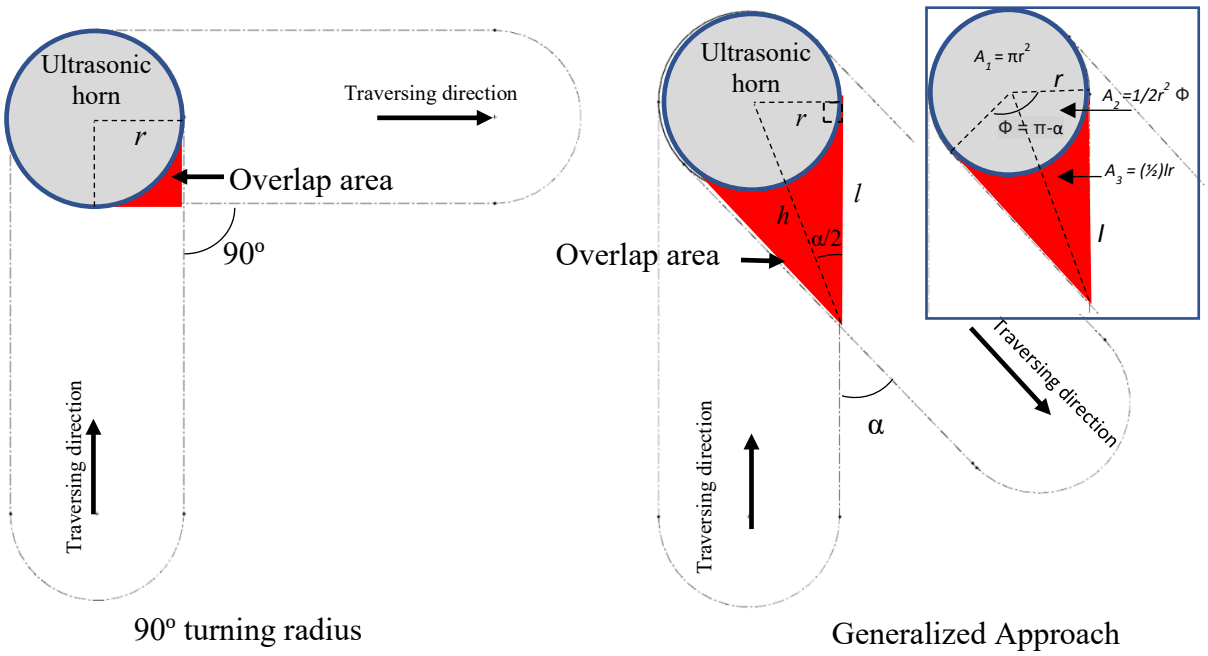

Figure 34 Overlap area and angle between segments

For the 90º turning radius shown in Figure 34, an overlap area (A) can be easily found using the following equation:

$$A_{90º overlap} = \pi r^2 + (r^2 - \frac{\pi r^2}{4}) \quad (10)$$

Equation 18 shows the overlap area where the section (shown in red from Figure 34) is heated twice. The following equations were used to obtain a generalized approach of the overlap area (A).

From trigonometry:

$$h = \frac{r}{sin\left(\frac{\propto}{2}\right)} \quad (11)$$

similarly,

$$l = h\cos\left(\frac{\propto}{2}\right) \quad (12)$$

Substituting h (equation 19) into equation 20 yields:

$$l = \left(\frac{r}{\sin\left(\frac{\propto}{2}\right)}\right)\cos\left(\frac{\propto}{2}\right) \qquad (13)$$

Simplifying yields to:

$$l = r\cot\left(\frac{\propto}{2}\right) \qquad (14)$$

Adding the areas to obtain the total area (A_T) from Figure 34,

$$A_T = A_1 + 2A_3 - A_2 \qquad (15)$$

Substituting A_1, A_2, and A_3 and simplifying yields,

$$A_T = r^2\left(\pi + \cot\left(\frac{\alpha}{2}\right) - \frac{1}{2}(\pi - \alpha)\right) \qquad (16)$$

Assuming that r is 1(unity) and substituting x for α in equation 24 yields,

$$f(x) = \pi + \cot\left(\frac{x}{2}\right) - \frac{1}{2}(\pi - x) \qquad (17)$$

The function was graphed along with its derivative using MATLAB:

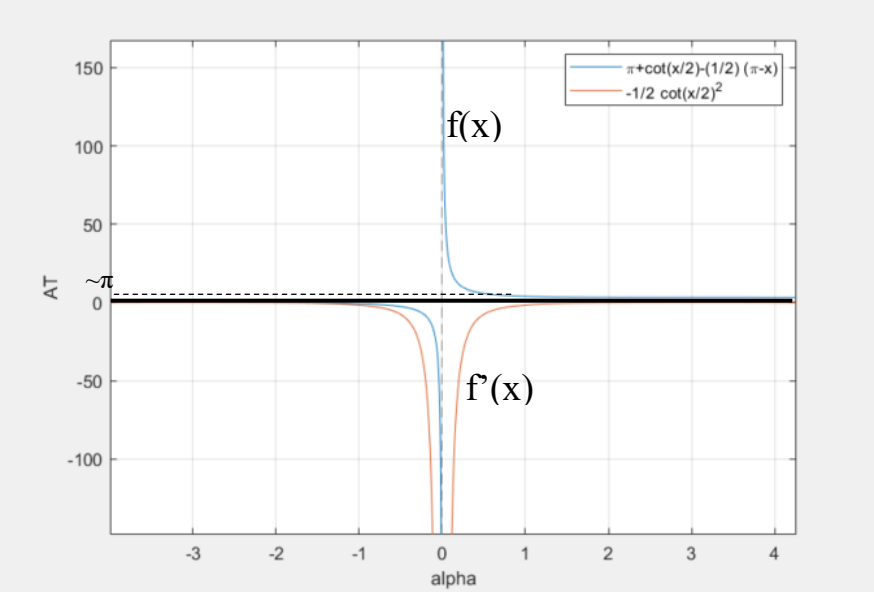

Figure 35 Indirect correlation between overlap area (AT) and angle (alpha) between segments

Figure 35 shows an indirect correlation between overlap area and angle between wire segments. The graph shows the minimum overlap area expressed by π or whenever f'(x) is equal to zero. However, if the turning angle (alpha) is reduced, the overlap area increases, therefore, embedding may not be possible due to the addition of excessive energy. The implementation of a close looped feedback wire embedding control with varying power input by varying the welding frequency and amplitude may be a continuation for this project to produce consistent wire embedding and obtain sharp turns with smaller arcs.

REFERENCES

Agarwala, M. K., Jamalabad, V. R., Langrana, N. A., Safari, A., Whalen, P. J., & Danforth, S. C. (1996). Structural quality of parts processed by fused deposition. *Rapid prototyping journal*, *2*(4), 4-19.

Bagsik, A., Schöppner, V., & Klemp, E. (2010, September). FDM part quality manufactured with Ultem* 9085. In *14th international scientific conference on polymeric materials* (Vol. 15, pp. 307-315).

Bailey, C. P. (2016). *G-code generation for multi-process 3D printing* (Doctoral dissertation, The University of Texas at El Paso). Bagsik, A., Schöppner, V., & Klemp, E. (2010, September). FDM part quality manufactured with Ultem* 9085. In *14th international scientific conference on polymeric materials* (Vol. 15, pp. 307-315).

Bayless, J., Chen, M., & Dai, B. (2010). Wire embedding 3D printer. *Engineering Physics Department, University of British Columbia*.

Bellini, A., Guceri, S., & Bertoldi, M. (2004). Liquefier dynamics in fused deposition. *Journal of Manufacturing Science and Engineering*, *126*(2), 237-246.

de Leon, A. C., Chen, Q., Palaganas, N. B., Palaganas, J. O., Manapat, J., & Advincula, R. C. (2016). High performance polymer nanocomposites for additive manufacturing applications. *Reactive and Functional Polymers*, *103*, 141-155.

Cengel, Y. A., & Ghajar, A. J. (2011). Heat and mass transfer (a practical approach, SI version).

De Vries, E. (2004). *Mechanics and mechanisms of ultrasonic metal welding* (Doctoral dissertation, The Ohio State University).

Diagne, M., Bekiaris-Liberis, N., & Krstic, M. (2017). Time-and State-Dependent Input Delay-Compensated Bang-Bang Control of a Screw Extruder for 3D Printing. *International Journal of Robust and Nonlinear Control*, *27*(17), 3727-3757.

Dudek, P. F. D. M. (2013). FDM 3D printing technology in manufacturing composite elements. *Archives of Metallurgy and Materials*, *58*(4), 1415-1418.

Espalin, D., Alberto Ramirez, J., Medina, F., & Wicker, R. (2014). Multi-material, multi-technology FDM: exploring build process variations. *Rapid Prototyping Journal*, *20*(3), 236-244.

Espalin, D., Muse, D. W., MacDonald, E., & Wicker, R. B. (2014). 3D Printing multifunctionality: structures with electronics. *International Journal of Advanced Manufacturing Technology*.

Fischer, F. (2011). Thermoplastics: the best choice for 3D printing. *White Paper, Stratasys Inc., Edn Prairie, MN*.

Gibson, I., Rosen, D. W., & Stucker, B. Additive manufacturing technologies. 2010. *Google Scholar*.

Jones, R., Haufe, P., Sells, E., Iravani, P., Olliver, V., Palmer, C., & Bowyer, A. (2011). RepRap–the replicating rapid prototyper. *Robotica*, *29*(1), 177-191.

Leigh, S. J., Bradley, R. J., Purssell, C. P., Billson, D. R., & Hutchins, D. A. (2012). A simple, low-cost conductive composite material for 3D printing of electronic sensors. *PloS one*, *7*(11), e49365.

Li, G., Zhao, J., Jiang, J., Jiang, H., Wu, W., & Tang, M. (2018). Ultrasonic strengthening improves tensile mechanical performance of fused deposition modeling 3D printing. *The International Journal of Advanced Manufacturing Technology*, 1-9.

Macdonald, E., Salas, R., Espalin, D., Perez, M., Aguilera, E., Muse, D., & Wicker, R. B. (2014). 3D printing for the rapid prototyping of structural electronics. *IEEE access*, *2*, 234-242.

MacDonald, E., & Wicker, R. (2016). Multiprocess 3D printing for increasing component functionality. *Science*, *353*(6307), aaf2093.

Masood, S., & Song, W. (2004). Development of new metal/polymer materials for rapid tooling using Fused deposition modelling . *Materials and Design 25*, 587-594.

Mohamed, O. A., Masood, S. H., & Bhowmik, J. L. (2015). Optimization of fused deposition modeling process parameters: a review of current research and future prospects. *Advances in Manufacturing*, *3*(1), 42-53.

Moylan, S., Slotwinski, J., Cooke, A., Jurrens, K., & Donmez, M. A. (2012, August). Proposal for a standardized test artifact for additive manufacturing machines and processes. In *Proceedings of the 2012 annual international solid freeform fabrication symposium* (pp. 6-8). Austin, TX.

Ning, F., Cong, W., Qiu, J., Wei, J., & Wang, S. (2015). Additive manufacturing of carbon fiber reinforced thermoplastic composites using fused deposition modeling. *Composites Part B: Engineering*, *80*, 369-378.

Perez, M. A., Ramos, J., Espalin, D., Hossain, M. S., & Wicker, R. B. (2013, August). Ranking model for 3D printers. In *Proceedings of the 2013 Solid Freeform Fabrication Symposium* (pp. 1048-1065).

Quinlan, H. E., Hasan, T., Jaddou, J., & Hart, A. J. (2017). Industrial and consumer uses of additive manufacturing: A discussion of capabilities, trajectories, and challenges. *Journal of Industrial Ecology*, *21*(S1), S15-S20.

Roberson, D., Espalin, D., & Wicker, R. (2013). 3D printer selection: A decision-making evaluation and ranking model. *Virtual and Physical Prototyping*, 201-212.

Rojas-Nastrucci, E. A., Ramirez, R., Hawatmeh, D., Lan, D., Wang, J., & Weller, T. (2017, September). Laser enhanced direct print additive manufacturing for mm-wave components and packaging. In *Electromagnetics in Advanced Applications (ICEAA), 2017 International Conference on* (pp. 1531-1534). IEEE.

Saari, M., Cox, B., Richer, E., Krueger, P. S., & Cohen, A. L. (2015). Fiber encapsulation additive manufacturing: An enabling technology for 3D printing of electromechanical devices and robotic components. *3D Printing and Additive Manufacturing*, *2*(1), 32-39.

Sato, K., Murayama, Y., Imada, S., & Shimokohbe, A. (1995). Control and elimination of lead screw backlash for ultra-precision positioning. *JSME international journal. Ser. C, Dynamics, control, robotics, design and manufacturing*, *38*(1), 36-41.

Shemelya, C., Cedillos, F., Aguilera, E., Espalin, D., Muse, D., Wicker, R., & MacDonald, E. (2015). Encapsulated copper wire and copper mesh capacitive sensing for 3-D printing applications. *IEEE Sensors Journal*, *15*(2), 1280-1286.

Shemelya, C., Cedillos, F., Aguilera, E., Maestas, E., Ramos, J., Espalin, D., ... & MacDonald, E. (2013, November). 3D printed capacitive sensors. In *SENSORS, 2013 IEEE* (pp. 1-4). IEEE.

Shemelya, C., Zemba, M., Liang, M., Yu, X., Espalin, D., Wicker, R., ... & MacDonald, E. (2016). Multi-layer archimedean spiral antenna fabricated using polymer extrusion 3D printing. *Microwave and Optical Technology Letters*, *58*(7), 1662-1666.

Shulman, H., Spradling, D., & Hoag, C. (2012). Introduction to additive manufacturing. *Ceramic Industry*, *162*(12), 15-19.

Siqueiros, J. G., Schnittker, K., & Roberson, D. A. (2016). ABS-maleated SEBS blend as a 3D printable material. *Virtual and Physical Prototyping*, *11*(2), 123-131.

Steenhuis, H. J., Ulusemre, T., & Fang, X. Technology Strategy and Developments in Consumer 3D Printers.

Suresh, K. S., Rani, M. R., Prakasan, K., & Rudramoorthy, R. (2007). Modeling of temperature distribution in ultrasonic welding of thermoplastics for various joint designs. *Journal of materials processing technology*, *186*(1-3), 138-146.

Tian, X., & Cao, Y. (2017). 3D printing for continous fiber reinforced thermoplastic compostites: Mechanism and performance. *Rapid Prototyping Journal*, 209-215.

Tian, X., Liu, T., Yang, C., Wang, Q., & Li, D. (2016). Interface and performance of 3D printed continuous carbon fiber reinforced PLA composites. *Composites Part A: Applied Science and Manufacturing*, *88*, 198-205.

Turner, B. N., & Gold, S. A. (2015). A review of melt extrusion additive manufacturing processes: II. Materials, dimensional accuracy, and surface roughness. *Rapid Prototyping Journal*, *21*(3), 250-261.

Turner, B. N., Strong, R., & Gold, S. A. (2013). A review of melt extrusion additive manufacturing processes: I. Process desing and modeling . *Rapid Prototyping Journal*, 192-204.

Ventola, C. L. (2014). Medical applications for 3D printing: current and projected uses. *Pharmacy and Therapeutics*, *39*(10), 704.

Wu, W., Geng, P., Li, G., Zhao, D., Zhang, H., & Zhao, J. (2015). Influence of layer thickness and raster angle on the mechanical properties of 3D-printed PEEK and a comparative mechanical study between PEEK and ABS. *Materials*, *8*(9), 5834-5846.

APPENDIX

APPENDIX A

Lead screw analysis

```
%Input the torque value and screw specifications
%0.1in travel screw

Tr= 2400; %Torque (N-mm) (input)
d=6.35; %major diameter (mm)
p=2.6; %pitch (mm)
n = 7; %number of engaged threads
dm = d-p/2 %mean diameter (mm)
l=p*n ; %lead (pitch*n)
alf=15.28*(pi/180)/2;%  2alf=thread angle
f=.16; %steel(machine oil) on bronze
Fr = 2*Tr*(pi*dm-f*l*sec(alf))/(dm*(1+pi*f*dm*sec(alf)));
%Force output per screw
Fmax=Fr*2 %maximum payload
Pounds= Fmax*0.22
```

Output:

Fmax =

6.9006e+03

Pounds =

1.5181e+03

Heat transfer Coefficient

```
g = 9.81; %acceleration due to gravity (m/s^3)
Ts = 120; %Surface temperature (C)
Tf = 24; %room temperature (C)
l = 0.22; %lenght of plate (m)
w= 0.17; %width of plate (m)
As = l*w; %Surface Area(m^2)
p = 2*l + 2*w; %perimeter
Pr = 0.7177; %Prantl number
lc = As/p; %characteristic length
v =1.995*10^-5 %Kinematic viscosity of air
k = 0.02 % Thermal conductivity of air (W/mK)

Tf= 1/2*(Ts+Tf) %film temperature
Beta= 1/Tf; %coeff of volm expansion

Ra = (g*Beta*(Ts-Tf)*lc^3)*Pr/v^2
Nu=0.54*Ra^(1/4)
h = Nu*k/lc %heat transfer coeff (w/m^2*k)
```

Output:

```
Nu =

    18.2341

h =

    7.6057
```

APPENDIX B
Repeatability tests

Table 8 X-axis Repeatability Tests (Machine 2mm travel)

Test #	lower value (mm)	Upper value (mm)
1	0.0000	1.89
2	0.0900	1.89
3	0.1000	1.89
4	0.1000	1.88
5	0.1000	1.88
6	0.1000	1.88
7	0.0900	1.88
8	0.0900	1.88
9	0.0900	1.88
10	0.0900	1.87

Table 9 Y-axis Repeatability Tests (Machine 2mm travel)

Test #	lower value (mm)	Upper value (mm)
1	0.00	2.02
2	0.24	2.00
3	0.25	2.00
4	0.25	2.00
5	0.25	2.00
6	0.25	2.00
7	0.26	2.00
8	0.26	2.00
9	0.26	2.00
10	0.26	2.00

Table 10 Z-axis Repeatability Tests (Machine 2mm travel)

Test #	lower value (mm)	Upper value (mm)
1	0	2.05
2	0	2.06
3	0	2.06
4	0	2.06
5	0.02	2.05
6	0.03	2.06
7	0.01	2.04
8	0.03	2.04
9	0.02	2.04
10	0.01	2.05

Table 11 Extruded lines measurements with digital caliper

Trial Number	**10 mm**	**20 mm**	**50 mm**	**100 mm**	**150 mm**
1	10.37	19.82	49.90	101.24	153.19
2	8.88	20.43	50.79	100.96	151.65
3	10.71	20.03	50.31	100.53	151.41
4	10.38	20.55	51.63	100.95	151.90
5	10.47	20.63	51.59	100.90	151.42
6	10.47	20.53	51.65	102.13	152.52
7	10.72	20.87	51.66	101.85	152.24
8	11.05	20.60	51.75	102.32	151.38
9	9.60	20.46	51.69	102.38	151.89
10	10.76	20.24	51.72	102.26	151.66

APPENDIX C

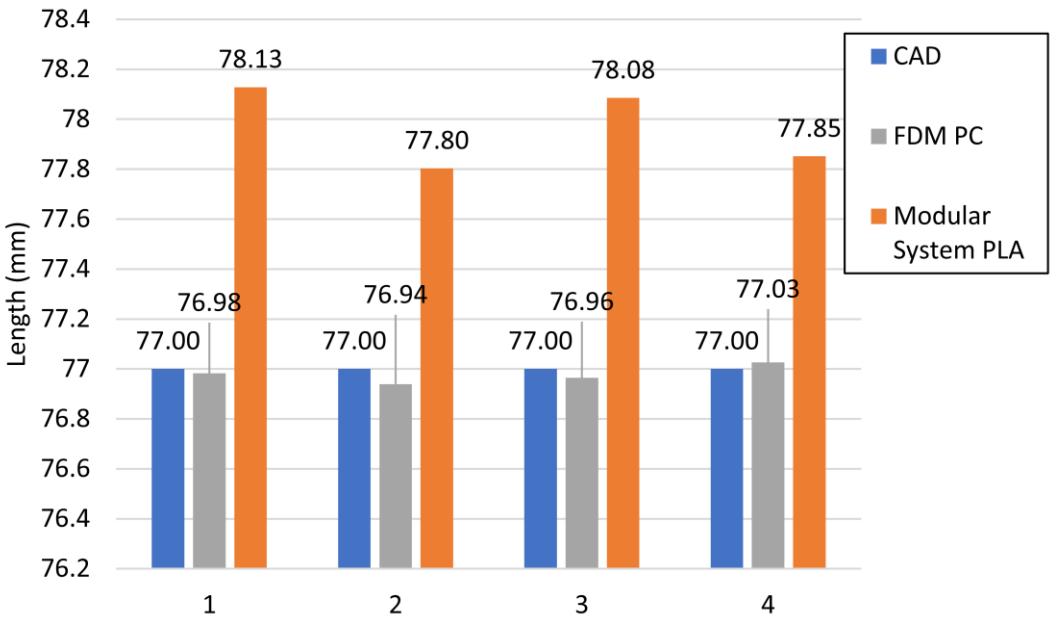

Figure 36 Graph showing the average length of each side of the ranking model. Comparison of CAD model, FDM industry grade 3D printer, and the developed modular 3D system.

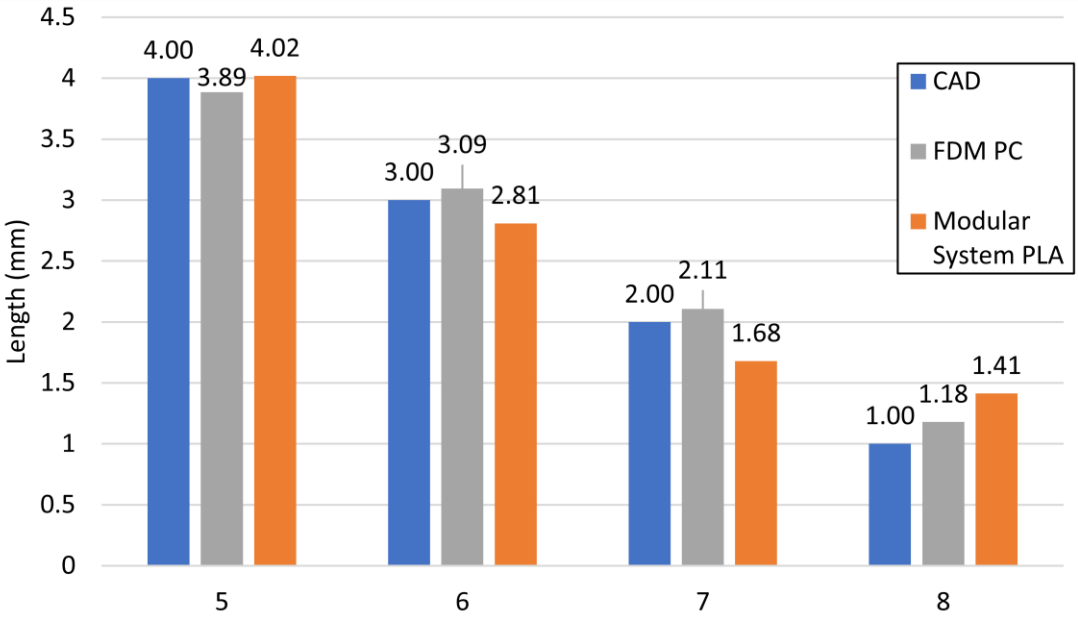

Figure 37 Graph showing the average in dimensions of circular extrusions with varying lengths. Comparison of CAD model, FDM industry grade 3D printer, and the developed modular 3D system.

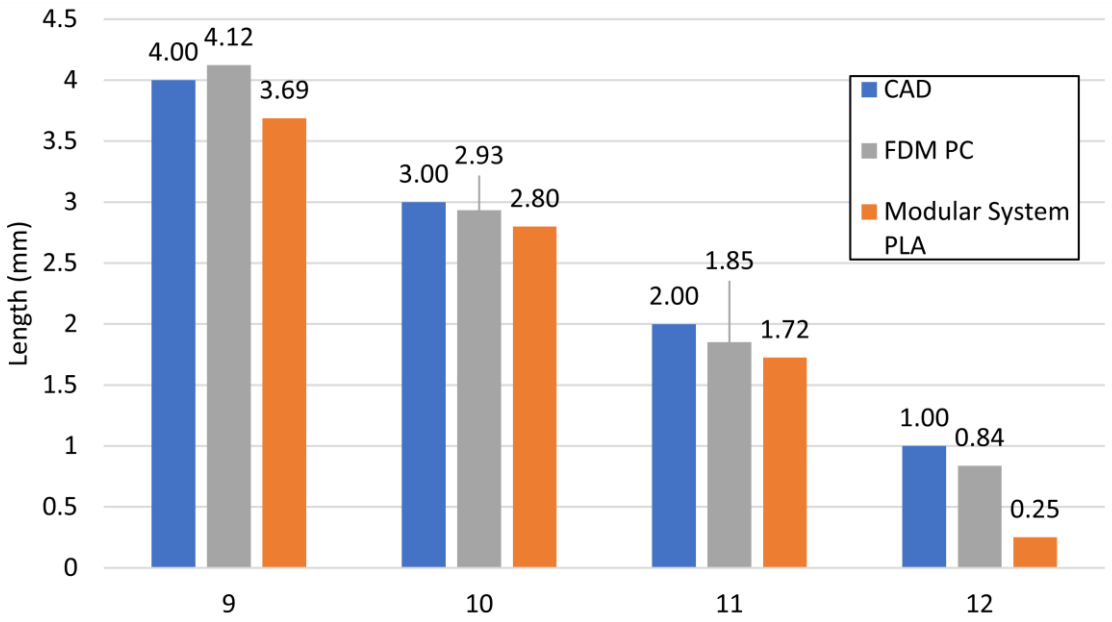

Figure 38 Graph showing the average in dimensions of circular cut extrusions with varying lengths. Comparison of CAD model, FDM industry grade 3D printer, and the developed modular 3D system.

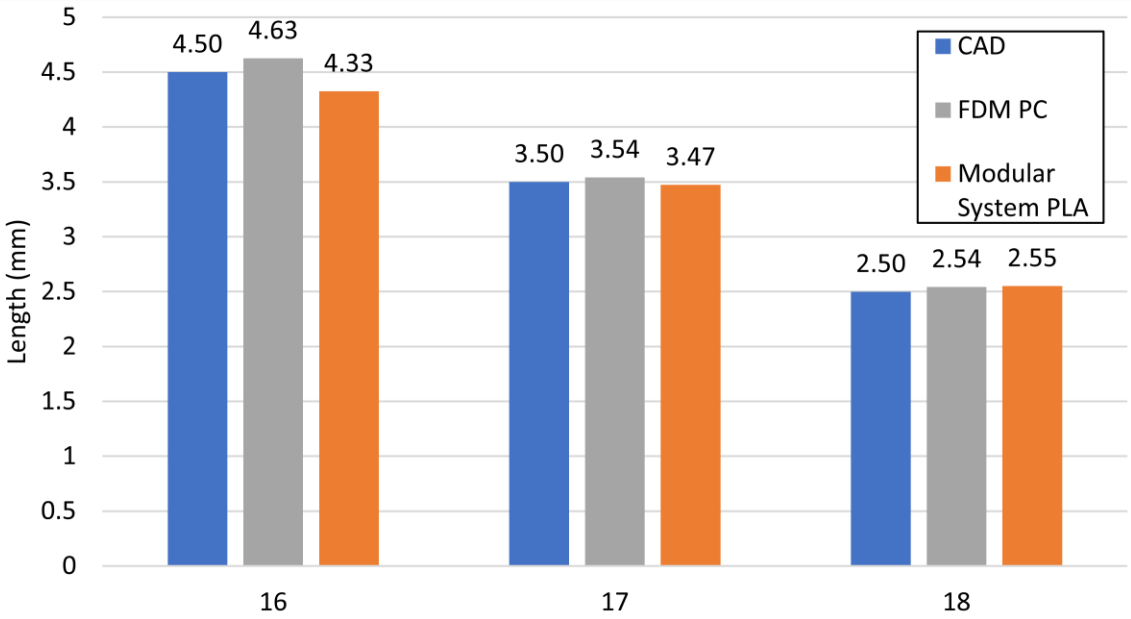

Figure 39 Graph showing the average in dimensions of square cut extrusions with varying lengths. Comparison of CAD model, FDM industry grade 3D printer, and the developed modular 3D system.

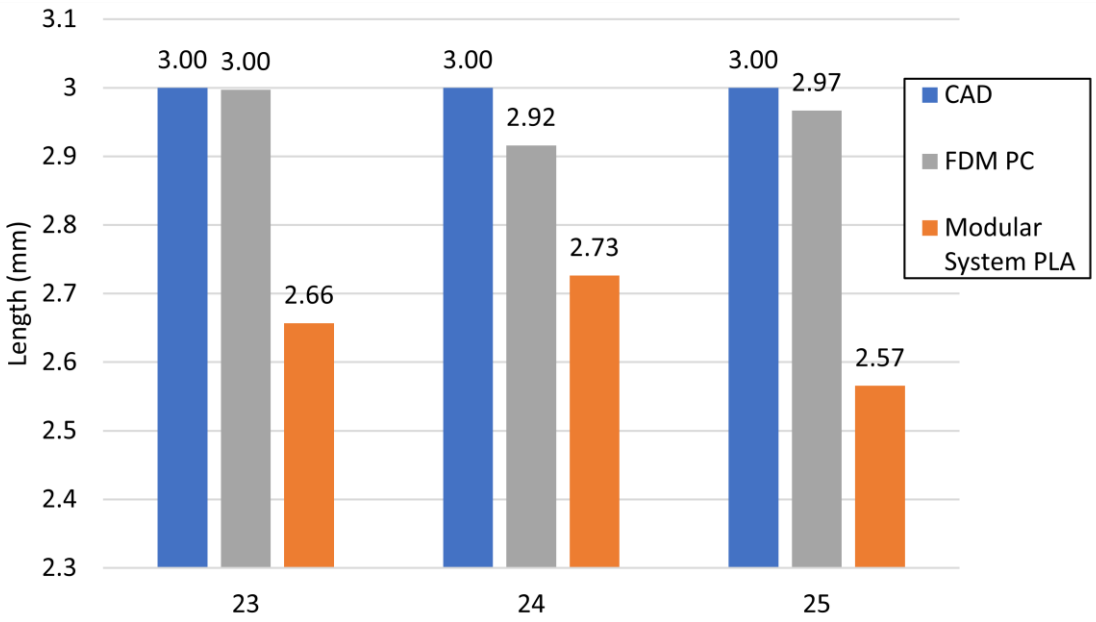

Figure 40 Graph showing the average in dimensions of circular cut extrusions the same diameter. Comparison of CAD model, FDM industry grade 3D printer, and the developed modular 3D system.

VITA

JOSE MOTTA was born in El Paso, TX, USA. He received the B.S. degree in mechanical engineering from The University of Texas at El Paso in 2015, where he will continue his PhD. degree in mechanical engineering. He is currently with the W.M. Keck Center for 3D innovation as a Graduate Research Assistant participating in the development of new technologies for material extrusion. He is involved in developing hybrid 3D printers to create multifunctional printed parts for the material extrusion process.

Contact Information: jfmotta@miners.utep.edu

This thesis/dissertation was typed by Jose Francisco Motta.